

Massive star formation in the GMC G345.5+1.0: Spatial distribution of the dust emission

Cristian López¹, Leonardo Bronfman¹, Lars-Åke Nyman², Jorge May¹, and Guido Garay¹

¹ Departamento de Astronomía, Universidad de Chile, Casilla 36-D, Santiago, Chile, e-mail: clopez@das.uchile.cl

² European Southern Observatory, Casilla 19001, Santiago, Chile.

ABSTRACT

Context. Massive condensations in giant molecular clouds (GMCs) are linked to the formation of high mass stars, which are the principal source of heavy elements and UV radiation, playing an important role in the evolution of galaxies.

Aims. We attempt to make a complete census of massive-star formation within all of GMC G345.5+1.0. This cloud is located one degree above the galactic plane and at 1.8 kpc from the Sun, thus there is little superposition of dust along the line-of-sight, minimizing confusion effects in identifying individual clumps.

Methods. We observed the 1.2 mm continuum emission across the whole GMC using the Swedish-ESO Submillimetre Telescope (SEST) Imaging Bolometer Array (SIMBA) mounted on the SEST. Observations have a spatial resolution of 0.2 pc and cover 1.8×2.2 in the sky with a noise of 20 mJy beam^{-1} .

Results. We identify 201 clumps with diameters between 0.2 and 0.6 pc, masses between 3.0 and $1.3 \times 10^3 M_{\odot}$, and densities between 5×10^3 and $4 \times 10^5 \text{ cm}^{-3}$. The total mass of the clumps is $1.2 \times 10^4 M_{\odot}$, thus the efficiency in forming these clumps, estimated as the ratio of the total clump mass to the total GMC mass, is ~ 0.02 . The clump mass distribution for masses between 10 and $10^3 M_{\odot}$ is well-fitted by a power law $dN/dM \propto M^{-\alpha}$, with a spectral mass index α of 1.7 ± 0.1 . Given their mass distribution, clumps do not appear to be the direct progenitors of single stars. Comparing the 1.2 mm continuum emission with infrared images taken by the Midcourse Space Experiment (MSX) and by the SPITZER satellite, we find that at least $\sim 20\%$ of the clumps are forming stars, and at most $\sim 80\%$ are starless. Six massive-star forming regions (MSFRs) embedded in clumps and associated with IRAS point sources have mean densities of $\sim 10^5 \text{ cm}^{-3}$, luminosities $> 10^3 L_{\odot}$, and spectral energy distributions that can be modeled with two dust components at different mean temperatures of 28 ± 5 and $200 \pm 10 \text{ K}$.

Key words. ISM: clouds – ISM: stars: formation – ISM: dust, extinction – ISM: stars: circumstellar matter

1. Introduction

1.1. Giant molecular clouds

High-mass stars are known to be born in massive and dense clumps embedded within giant molecular clouds (GMCs; Zinnecker & Yorke 2007). These GMCs have typical radii of $\sim 60 \text{ pc}$, masses of $10^6 M_{\odot}$ and temperatures of $\sim 10 \text{ K}$, and are found to be concentrated toward the Galactic plane (Grabelsky et al. 1988). This gives rise to spatial and kinematic blending along the line-of-sight. For example, the CO emission, the most frequently used tracer of molecular gas for GMCs, with a low critical density ($\sim 10^2 \text{ cm}^{-3}$), is often complex with multiple profile components. To overcome these observational difficulties and perform a complete census of massive-star forming regions (MSFRs) in a whole GMC, ideally requires one to study GMCs above and below the Galactic plane using a high density tracer. Recent surveys of dust condensations within whole GMCs have been made toward RCW 106 (Mookerjee et al. 2004), Cygnus X (Motte et al. 2007), and NGC 6334 (Muñoz et al. 2007) using millimeter continuum emission as a high density tracer.

1.2. Massive-star forming regions

MSFRs are embedded in GMCs, generating a high Lyman continuum photon flux ($\gtrsim 2 \times 10^{45} \text{ photons sec}^{-1}$; Panagia 1973) that ionizes the surrounding gas and heats the surrounding dust. These MSFRs can thus be identified by infrared emission from heated dust and/or by radio emission from ionized gas. They can

also be identified based on both their molecular lines from high density gas and their millimeter and sub-millimeter continuum emission from dust.

Bronfman et al. (1996) showed that 60% of the IRAS point sources in the Galactic plane with far infrared (FIR) colors typical of ultra compact (UC) HII regions (Wood & Churchwell 1989) are associated with dense molecular structures seen in the CS(2-1) line ($\gtrsim 10^4\text{--}10^5 \text{ cm}^{-3}$). Hereafter, these sources will be referred to as IRAS-CS sources. From observations in 1.2 mm continuum emission of 146 IRAS-CS sources, Faúndez et al. (2004) showed that MSFRs are associated with condensations of gas and dust. Infrared studies, however, cannot provide a complete census of the birth sites of massive stars, since there are massive condensations that are undetected at infrared wavelengths. For example, Garay et al. (2004) found four clumps with masses between 4×10^2 and $2 \times 10^3 M_{\odot}$ and densities of $\sim 2 \times 10^5 \text{ cm}^{-3}$, without infrared emission, located close to clumps associated with MSFRs. They suggested that these cold ($\lesssim 17 \text{ K}$), dense, and massive clumps will eventually form high mass stars. Hill et al. (2005) found 113 cold clumps, which have a mean mass of $\sim 800 M_{\odot}$, a mean radius of $\sim 0.4 \text{ pc}$, and a mean density of $\sim 10^5 \text{ cm}^{-3}$. Beltrán et al. (2006) found 95 cold clumps with a mean mass of $96 M_{\odot}$, a mean radius of 0.4 pc , and a mean density of $9 \times 10^4 \text{ cm}^{-3}$.

1.3. Clumps in GMCs

Observations in molecular lines (e.g. Bains et al. 2006) and dust continuum emission (e.g. Muñoz et al. 2007) on spatial scales smaller than ~ 1 pc show that GMCs have a fragmented structure, and these sub-structures have been referred to as clumps (Williams et al. 2000).

Clumps in GMCs have masses from 4 to $10^4 M_\odot$, diameters from 0.2 to 2 pc, and densities from 10^3 to 10^5 cm^{-3} . The clump mass distribution is consistent with a power law $dN/dM \propto M^{-\alpha}$, where dN/dM is the number of objects by mass interval, M is the mass, and α is the mass spectral index. The derived mass spectral indices range between 1.3 and 1.8 (e.g. Mookerjee et al. 2004; Muñoz et al. 2007), values similar to those found for the mass distribution of molecular clouds as a whole ($\alpha=1.5$ -1.6; Sanders et al. 1985; Solomon et al. 1987; Williams & McKee 1997). The similarity between the spectral mass indices suggests a common origin; however, different mechanisms have been proposed to explain the formation of clumps and GMCs. On the one hand, large-scale gravitational instabilities, in the combined medium of the collisionless stars and the collisional gas, drive spiral density waves (e.g. Li et al. 2005), and are likely to be the main mechanism behind GMC formation. On the other hand, since GMCs are considered turbulent and supersonic, it is expected that the clump formation is, to first order, produced by ram pressures from supersonic flows, which can provide the seeds for a gravitational fragmentation (Ballesteros-Paredes et al. 2006 and 2007; Bonnell et al. 2007; Klessen et al. 1998).

1.4. This paper

To undertake a complete census of dense and massive clumps, including those with and without infrared emission, we observed the whole of GMC G345.5+1.0 in 1.2 mm continuum emission. The determination of physical properties of a sample of clumps belonging to a single GMC is desirable since, in this way, the distance to the GMC is a factor that influences neither the mass distribution or the relationships between physical properties. However, these studies are difficult because of the superposition of dust and molecular structures along the line-of-sight to GMCs in the Galactic plane. We chose the GMC G345.5+1.0 as our target for two reasons. First, it is located $\sim 1^\circ$ above the Galactic plane, so our observations in the 1.2 mm continuum emission and in the $^{13}\text{CO}(3-2)$ line are roughly free of confusion with background or foreground structures along the line-of-sight. Second, it is at 1.8 kpc from the Sun, near enough to resolve clumps associated with MSFRs, but far enough away to permit a complete coverage of the GMC.

The structure of this article is as follows: Sections 2 and 3 present, respectively, the main characteristics of G345.5+1.0 and the observations; Section 4 presents the results and a discussion, and Sect. 5 gives a summary of our study.

2. GMC G345.5+1.0

The GMC G345.5+1.0 was first observed as part of the Columbia University - Universidad de Chile $^{12}\text{CO}(1-0)$ Survey of the Southern Galaxy (Bronfman et al. 1989). It is located approximately between 344.5° and 346.5° in Galactic longitude, and between 0.2° and 2.0° in Galactic latitude. Figure 1 shows the spectrum of the $^{12}\text{CO}(1-0)$ line emission integrated over the area of the GMC. The emission of the GMC is between -33 and -2 km s^{-1} (LSR velocities) with a peak at -13.6 km s^{-1} .

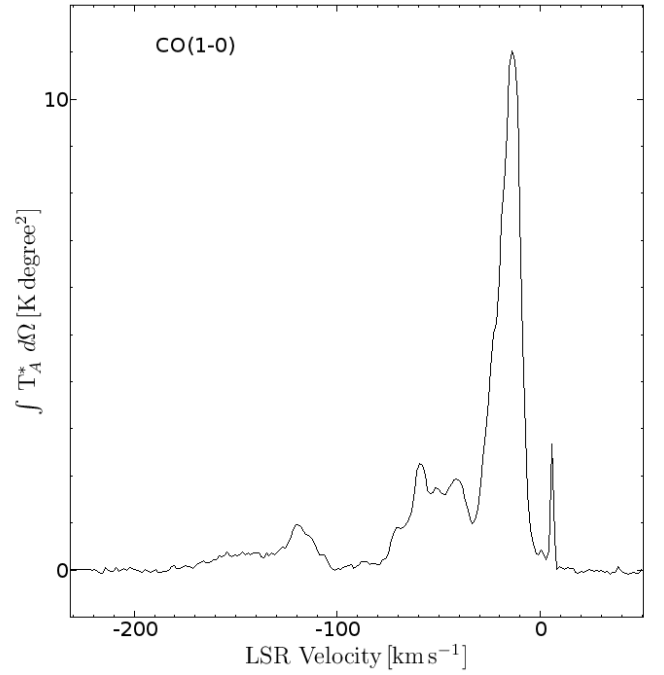


Fig. 1. Spectra of the $^{12}\text{CO}(1-0)$ line emission integrated over the whole area of the GMC G345.5+1.0 (between 344.5° and 346.5° in Galactic longitude and between 0.2° and 2.0° in Galactic latitude; Bronfman et al. 1989). Emission from the GMC under study is between -33 and -2 km s^{-1} with a peak at -13.6 km s^{-1} .

Table 1. Summary of main characteristics of G345.5+1.0.

Distance	1.8 kpc
Total mass	$6.5 \times 10^5 M_\odot$
Radius	34 pc
^a Density	70 cm^{-3}
^a Column density	10^{22} cm^{-2}
LSR velocity	-13.6 km s^{-1} (between -33 and -2 km s^{-1})

^a The density and the column density are computed assuming a mean molecular weight of $\mu=2.29$.

We estimate the kinematic distance using the rotation curve determined by Alvarez et al. (1990), with a Galactocentric solar distance of 8.5 kpc and a solar LSR velocity of 220 km s^{-1} . Considering a Galactic longitude of 345.5° and LSR velocity of -13.6 km s^{-1} , the GMC is within the solar circle with two possible kinematic distances: ~ 1.8 and 15 kpc. Thus, the GMC is ~ 31 or 262 pc above the Galactic plane, a factor 0.5 or 4.4 of the HWHM of the molecular Galactic disk (~ 60 pc; Bronfman et al. 2000), respectively. Therefore, 1.8 kpc is the most probable kinematic distance to the GMC.

Physical properties of the GMC are estimated using the $^{12}\text{CO}(1-0)$ line observations. The $^{12}\text{CO}(1-0)$ line emission integrated over the full spatial and spectral extension of the GMC is $192 \text{ K km s}^{-1} \text{ deg}^2$. Using a ratio of H_2 column density to integrated $^{12}\text{CO}(1-0)$ line emission $N_{\text{H}_2}/W_{\text{CO}}$ equal to $1.56 \times 10^{20} \text{ cm}^{-2} (\text{K km s}^{-1})^{-1}$ (Hunter et al. 1997), the total mass of the GMC is $6.3 \times 10^5 M_\odot$, corrected by a factor of 1.3 to account for 25% of helium. Since its angular size is $2.0^\circ \times 1.8^\circ$, the GMC has a mean radius of ~ 34 pc, mean column density of $\sim 10^{22} \text{ cm}^{-2}$ and mean density of $\sim 70 \text{ cm}^{-3}$, where the depth of the cloud has been assumed to be same as its radius. Table 1

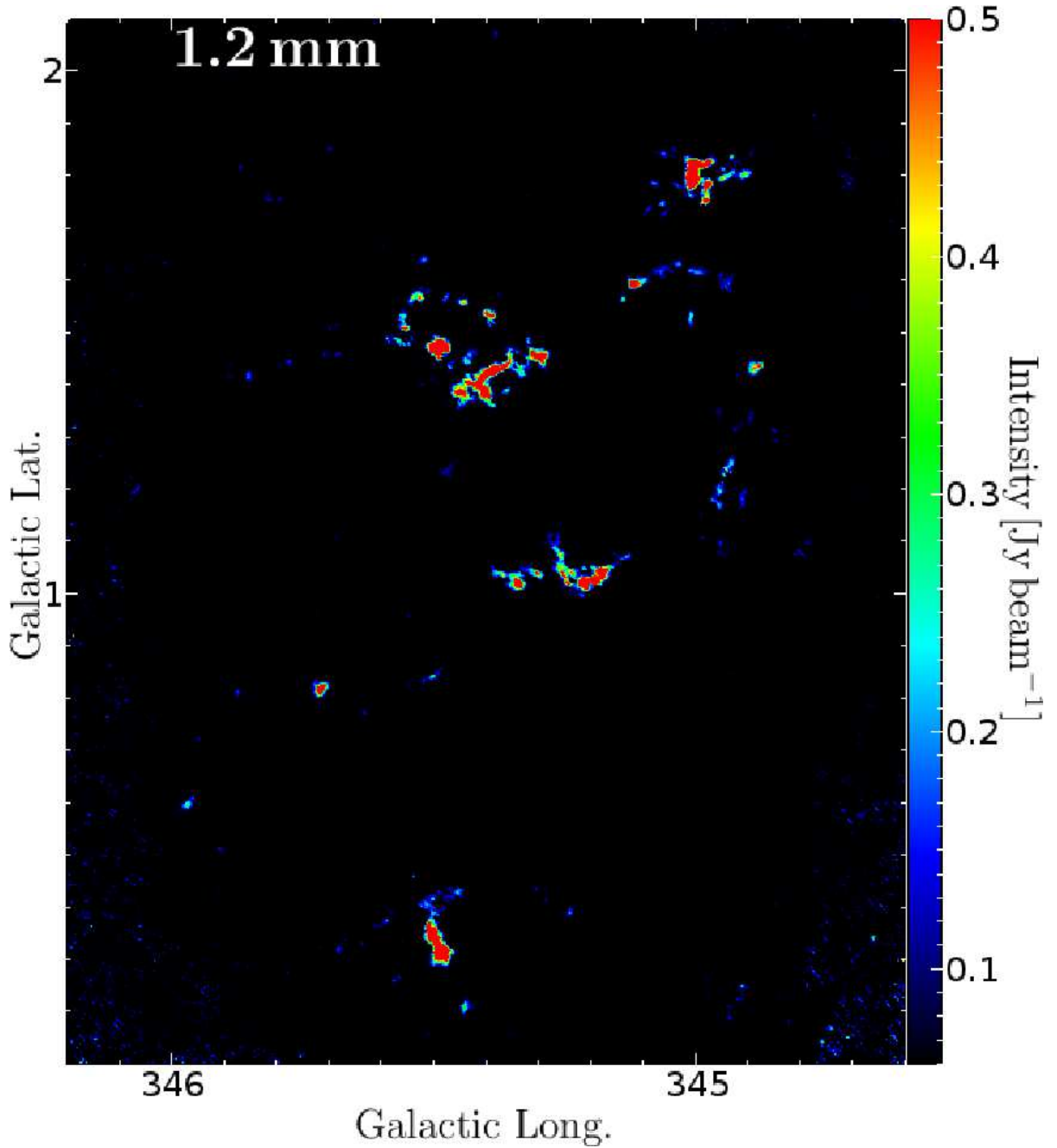


Fig. 2. Map of the GMC G345.5+1.0 in 1.2 mm continuum emission. Observations were made using SIMBA, with a spatial resolution of 0.2 pc. They cover $1^{\circ}8 \times 2^{\circ}2$ in the sky, with an rms of 20 mJy beam^{-1} .

summarises the main characteristics of this GMC. The derived physical properties confirm that the most probable distance to the GMC is $\sim 1.8 \text{ kpc}$. If at the far kinematic distance (15 kpc), the GMC would have a mean radius of 280 pc and a total mass of $4.4 \times 10^7 M_{\odot}$, values much higher than the typical value of 60 pc in radius and $10^6 M_{\odot}$ in mass (Dame et al. 1986); Williams & McKee (1997) found that the molecular cloud mass distribution within the solar circle has an upper mass limit of $6 \times 10^6 M_{\odot}$.

3. Observations

We observed the whole GMC G345.5+1.0 in continuum emission at 1.2 mm using SIMBA mounted on the SEST. The SEST is a 15-m diameter radio telescope, which operated between 70

and 365 GHz, and SIMBA is a 37-channel hexagonal bolometer, operating at 250 GHz (1.2 mm), with a passband equivalent width of 90 GHz (FWHM). The configuration SEST-SIMBA had a beamsize of $24''$, which corresponds to a spatial resolution of $\sim 0.2 \text{ pc}$ at the GMC distance (1.8 kpc).

Observations were made in October 2002 and July 2003, using the fast mapping mode, and consist of 185 images of $15'$ (azimuth) $\times 10'$ (elevation) in size. The scans were made in azimuth at a rate of $80'' \text{ s}^{-1}$, and they were separated in elevation by $8''$; the total integration time per map was about 25 minutes. Measurements of the atmospheric opacity were made through skydips about every three hours, and values at the zenith ranged between 0.09 and 0.31. Data were reduced using the MOPSI software (developed by Robert Zylka, IRAM, Grenoble,

Table 2. List of IRAS point sources along the line-of-sight to the GMC G345.5+1.0 observed in the CS(2-1) line by Bronfman et al. (1996).

IRAS name	Galactic coord.		LSR velocity ¹	FWHM ¹
	longitude	latitude	[km s ⁻¹]	[km s ⁻¹]
16533-4022	344.845	1.646	undetected	
16571-4029	345.208	1.028	-15.6	4.9
16577-4028	345.286	0.933	undetected	
16575-4023	345.332	1.014	-14.5	2.8
16561-4006	345.393	1.399	-11.9	3.5
16557-4002	345.395	1.512	-12.4	3.1
17009-4042	345.490	0.311	-16.7	6.0
16562-3959	345.494	1.468	-11.6	5.5
17008-4040	345.499	0.354	-16.4	4.8
16596-4012	345.717	0.817	-11.5	4.9

¹ Values from Bronfman et al. (1996).

France), and calibrated (in terms of flux density) with observations toward Uranus, one made in October 2002, and an additional eight made in July 2003. Bolometer channels were corrected for the correlated noise by inspecting the surrounding channels. The noise correlation between 1 and 900 arcsec, and between 100 and 900 arcsec inferred an uncertainty/error smaller than 20% in the flux densities of detected sources. The calibration factor has a value of 0.086 Jy counts⁻¹ for October 2002, and a mean value of $\sim 0.069 \pm 0.005$ Jy counts⁻¹ for July 2003. These variations agree with the uncertainty estimated by Faúndez et al. (2004) of 20% in the flux density measurements using SIMBA data.

For the 185 images, we achieved an rms of between 0.023 and 0.080 Jy beam⁻¹, with a median of 0.036 Jy beam⁻¹, for a beam calibration area of ~ 653 arcsec² (“SIMBA Data Reduction Handbook”). The individual maps were combined in a mosaic of 1.8×2.2 in size, centered at 345°40 in Galactic longitude and +1°10 in Galactic latitude, and with a final rms of ~ 20 mJy beam⁻¹.

4. Results and discussion

4.1. The 1.2 mm continuum emission

Figure 2 presents the 1.2 mm emission image of the whole GMC G345.5+1.0. The total flux density of the GMC G345.5+1.0 is ~ 365 Jy, which is estimated by integrating the intensity over the whole area of the cloud.

As can be seen in the integrated spectrum of the ¹²CO(1-0) line (Fig. 1), across GMC G345.5+1.0 (LSR velocity between -33 and -2 km s⁻¹), there are additional molecular gas components along the line-of-sight, particularly in the ranges -170 to -100 km s⁻¹, -75 to -33 km s⁻¹, and 0 to 5 km s⁻¹. Hence, the question arises as to whether the 1.2 mm continuum emission only traces dust condensations within GMC G345.5+1.0? To examine the association of the GMC with 1.2 mm continuum emission, Fig. 3 shows images of the velocity-integrated ¹²CO(1-0) emission in three velocity ranges (-200 to -33 km s⁻¹, -33 to -2 km s⁻¹, and -2 to 50 km s⁻¹) superimposed with contours of the 1.2 mm continuum emission. Figure 3 shows that most of the emission detected in 1.2 mm is associated with the GMC. About 1% of the total observed area might also be associated with gas at

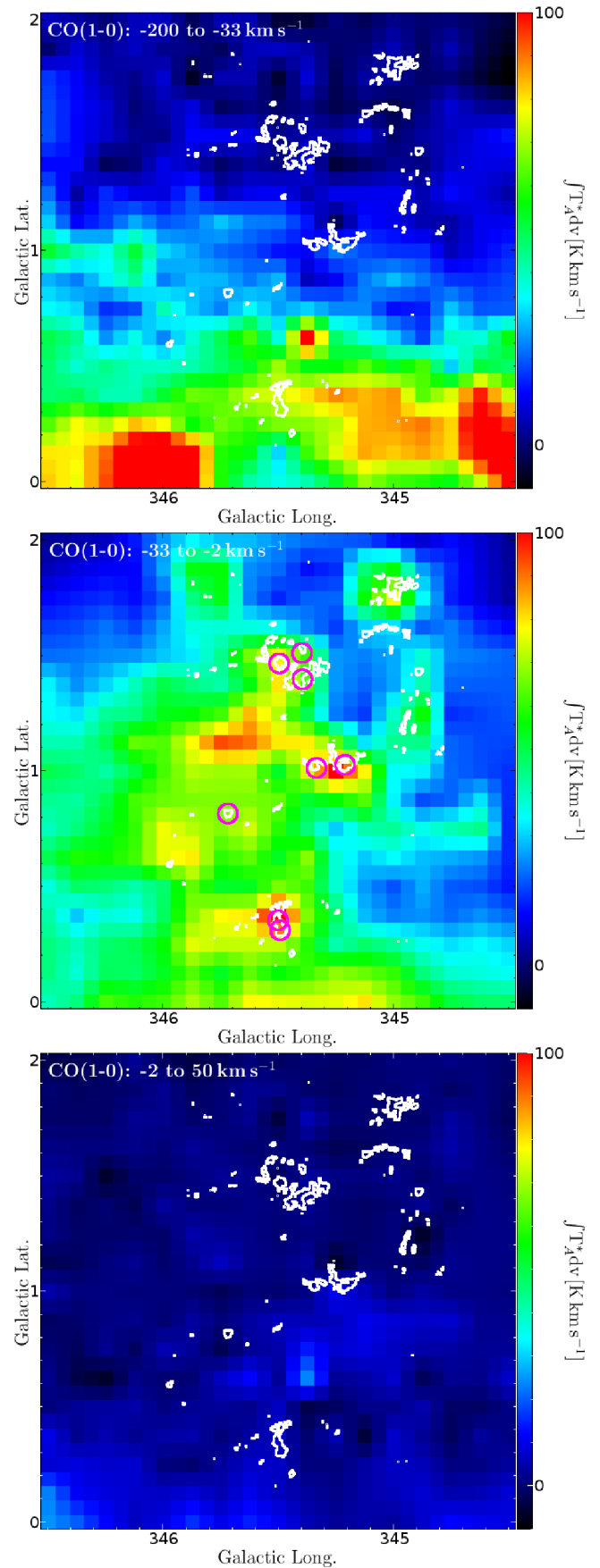


Fig. 3. Integrated ¹²CO(1-0) emission toward GMC G345.5+1.0 in different LSR velocity ranges (Bronfman et al. 1989). Top: from -200 to -33 km s⁻¹. Middle: from -33 to -2 km s⁻¹. Bottom: from -2 to 50 km s⁻¹. Magenta circles mark spatial and spectral positions of detections in the CS(2-1) line toward MSFRs (Table 2). Contours represent 1.2 mm continuum emission at 5 times rms, ~ 0.1 Jy beam⁻¹.

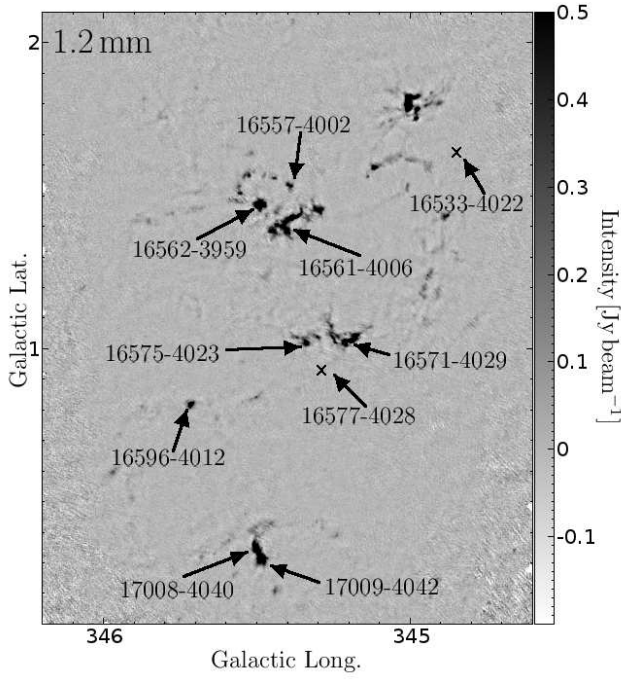


Fig. 4. IRAS point sources along the line-of-sight of the GMC G345.5+1.0 observed in the CS(2-1) line (Bronfman et al. 1996). Gray scale represents 1.2 mm continuum emission. Arrows mark CS(2-1) line observations, and crosses indicate observations without detection (see Table 2).

velocities $< -33 \text{ km s}^{-1}$ (Fig. 3, top), localized mainly in the region of the IRAS point sources 17008-4040 (G345.499+0.354) and 17009-4042 (G345.490+0.311).

From the survey of Bronfman et al. (1996), we find that there are eight IRAS-CS sources within the region and two IRAS point sources that are not detected in the CS(2-1) line (see Table 2). As is shown in both the $^{12}\text{CO}(1-0)$ maps (Fig. 3) and the 1.2 mm continuum emission map (Fig. 4), these MSFRs, or IRAS-CS sources, are associated with the GMC and have a counterpart in 1.2 mm. They correspond to the most dense and massive dust condensations (see Table 5). The two IRAS point sources not detected in the CS(2-1) line were also not detected in the continuum (see Fig. 4). The eight IRAS-CS sources include the IRAS point sources 17008-4040 and 17009-4042. Line profiles toward these two objects in the $^{12}\text{CO}(1-0)$ and CS(2-1) lines are shown in Fig. 5. Gas components with velocities $< -33 \text{ km s}^{-1}$ observed in the $^{12}\text{CO}(1-0)$ line are not observed in the CS(2-1) line, suggesting that they correspond to regions of low density gas. Since 1.2 mm continuum emission traces high densities (e.g. Faúndez et al. 2004), it should not be detected in these clouds. In summary, from observations in the $^{12}\text{CO}(1-0)$ and CS(2-1) lines, we conclude that the 1.2 mm continuum emission is associated only with the GMC.

4.2. Identification of clumps

The structure of the GMC observed in 1.2 mm continuum emission (Fig. 2) is fragmented, and it is possible to distinguish several clumps.

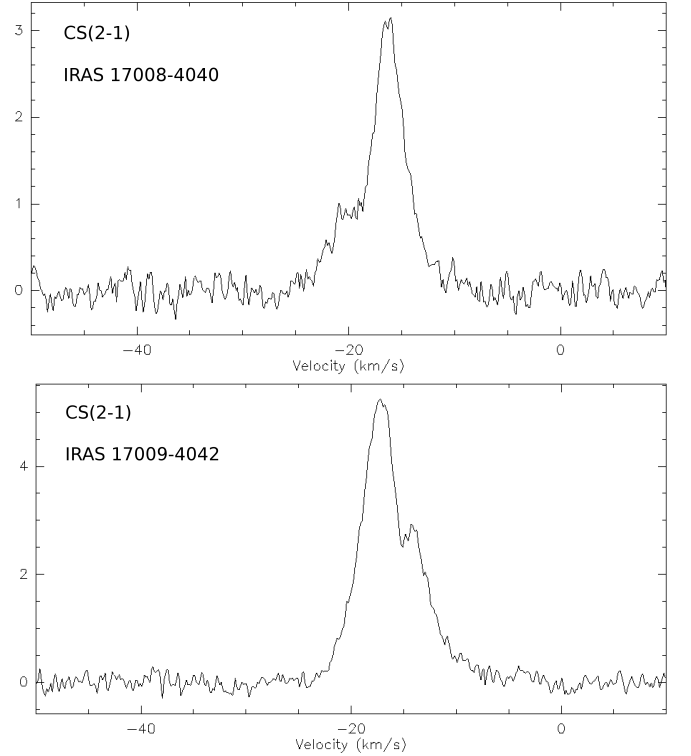
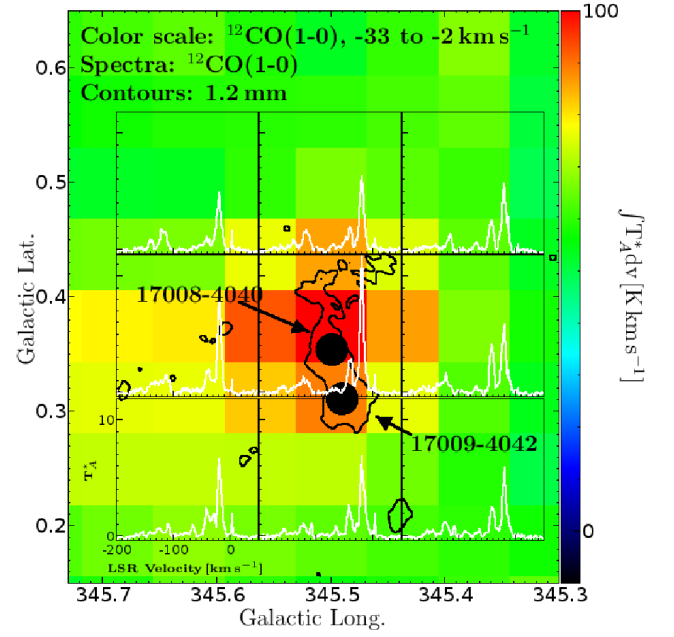


Fig. 5. Line profiles toward the IRAS point sources 17008-4040 and 17009-4042: top image, $^{12}\text{CO}(1-0)$ line profiles (Bronfman et al. 1989), over a map of their integrated emissions (color scale) and with contours of 1.2 mm continuum emission; middle and bottom images, CS(2-1) line profiles (their observing positions are indicated as black dots in the top image; Bronfman et al. 1996).

To identify clumps we utilize CLUMPFIND¹ (Williams et al. 1994), which creates contours over data, searches for peaks of emission to locate clumps, and follows them down to the lower intensity contour.

¹ <http://www.ifa.hawaii.edu/users/jpw/clumpfind.shtml>

CLUMPFIND finds 201 clumps in the 1.2 mm continuum emission map of the GMC, containing $\sim 100\%$ of the total emission above 3σ . We used a lower intensity contour of three rms, $\sim 0.06 \text{ Jy beam}^{-1}$, and a contouring interval equal to twice the rms noise, $\sim 0.04 \text{ Jy beam}^{-1}$. To delete fictitious structures, we imposed two conditions on the CLUMPFIND output, that the angular size of the emission and the emission peak of clumps had to be greater than the beam size, $\sim 24'' \times 24''$, and five times rms, $\sim 0.1 \text{ Jy beam}^{-1}$, respectively. The angular size is defined to be the angular area inside the lowest intensity contour (three rms). The 201 identified clumps have areas between ~ 0.18 and 7.3 arcmin^2 , emission peaks between 0.1 and 9 Jy beam^{-1} , and flux densities between 0.089 and 40 Jy .

Table 5, available online in electronic form at the publishers² (EDP Sciences), shows the characteristics of each clump calculated in this section, Sect. 4.3 and Sect. 4.4. Column 1 gives clump names; columns 2 and 3, Galactic coordinates of peaks in 1.2 mm continuum emission; column 4, 1.2 mm flux densities; column 5, diameters (deconvolved FWHM sizes); column 6, masses; column 7, densities; column 8, column densities; and column 9, if clumps have ("Y") or do not have ("N") an infrared counterpart from MSX and SPITZER observations.

4.3. Physical properties of clumps

First, we estimate the minimum gas column density that can be detected given the rms noise of our observations. Assuming that 1.2 mm continuum emission is optically thin and produced by dust, the column density N is (Hildebrand 1983)

$$N = \frac{S_{1.2\text{mm}} R_{gd}}{\Omega \mu m_H k_{1.2\text{mm}} B_{1.2\text{mm}}(T_{\text{dust}})}, \quad (1)$$

where Ω is the beam solid angle, $S_{1.2\text{mm}}$ is the flux density at 1.2 mm, μ is the mean mass per particle, equal to ~ 2.29 for an H_2 cloud with a 25% contribution of helium (Evans 1999), m_H is the hydrogen atom mass, $k_{1.2\text{mm}}$ is the dust absorption coefficient at 1.2 mm, equal to $\sim 1 \text{ cm}^2 \text{ g}^{-1}$ for protostellar cores (Ossenkopf & Henning 1994), $B_{1.2\text{mm}}(T_{\text{dust}})$ is the Planck function at both 1.2 mm and a dust temperature T_{dust} , equal to $\sim 30 \text{ K}$ for regions of massive-star formation (Faúndez et al. 2004), and R_{gd} is the ratio of gas to dust mass, ~ 100 (Hildebrand 1983). For a solid angle limit of $24'' \times 24''$ and an intensity limit of five rms, $\sim 0.1 \text{ Jy beam}^{-1}$, the minimum flux density is $\sim 88 \text{ mJy}$ and the minimum column density that can be detected is $\sim 4 \times 10^{21} \text{ cm}^{-2}$, which corresponds to a visual extinction of 4 mag, assuming that $N_{\text{H}_2}/A_V \sim 10^{21} \text{ cm}^{-2} \text{ mag}^{-1}$ (Bohlin et al. 1978).

Masses of clumps, M_c , are estimated as

$$M_c = \int \mu m_H N dA = \frac{S_{1.2\text{mm}} R_{gd} d^2}{B_{1.2\text{mm}}(T_{\text{dust}}) k_{1.2\text{mm}}},$$

where dA is the differential element of area ($dA = d^2 d\Omega$) and d is the distance to the GMC ($\sim 1.8 \text{ kpc}$). Since we insist that identified clumps have intensities and dimensions greater than 0.1 Jy beam^{-1} and $24'' \times 24''$ respectively, the lower limit to their masses is $\sim 2.9 M_\odot$. The derived masses of clumps range from 3.0 to $1.3 \times 10^3 M_\odot$, with a total mass of $1.2 \times 10^4 M_\odot$ (see Tables 3 and 5). The efficiency in forming these clumps, estimated as the ratio of the total clump mass to the total GMC mass, is thus ~ 0.02 .

The clump mass distribution (CMD) is shown in Fig. 6, plotted as $dN/d \log(M/M_\odot)$ versus mass, where $dN/d \log(M/M_\odot)$

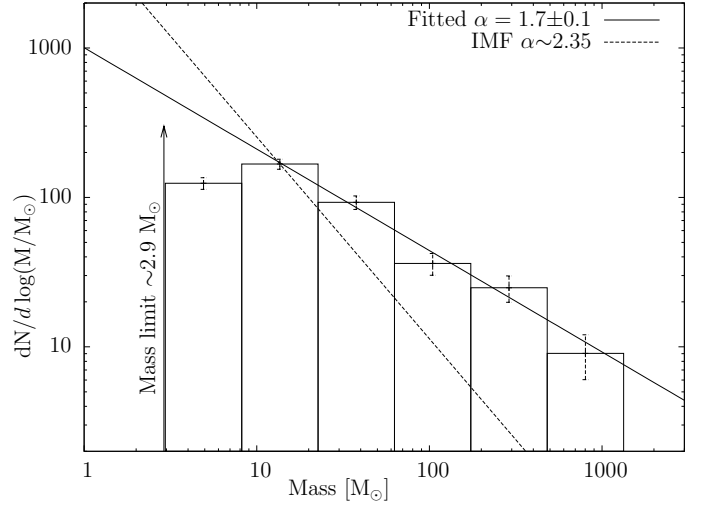


Fig. 6. Mass distribution of identified clumps in G345.5+1.0, plotted as $dN/d \log(M/M_\odot)$ versus mass, where $dN/d \log(M/M_\odot)$ is approximated by the number of clumps ΔN within a logarithmic mass interval $\Delta \log(M/M_\odot)$. Here, $\Delta \log(M/M_\odot)$ is constant, ~ 0.44 . Error bars are estimated by $\sqrt{\Delta N / \Delta \log(M/M_\odot)}$. The arrow shows the clump mass limit, $\sim 2.9 M_\odot$. The continuous line represents the mass distribution fit with $dN/d \log(M/M_\odot) \propto M^{1-\alpha}$, where the spectral mass index α is 1.7 ± 0.1 for masses between ~ 10 and $1.3 \times 10^3 M_\odot$. The dashed line displays the spectral mass index for the stellar initial mass function (IMF) of the solar neighborhood for stellar masses greater than $0.5 M_\odot$ (e.g. Kroupa 2002); the line is forced to pass through the peak of the clump mass distribution.

is approximated by the number of clumps, ΔN , within a logarithmic mass interval $\Delta \log(M/M_\odot)$. In this figure, $\Delta \log(M/M_\odot)$ is constant, at a value of ~ 0.44 . The CMD is well-fitted by a power law $dN/d \log(M) \propto M^{-\alpha+1}$, which can be expressed as $dN/dM \propto M^{-\alpha}$, with the spectral mass index, α , equal to 1.7 ± 0.1 for masses between ~ 10 and $1.3 \times 10^3 M_\odot$. The correlation coefficient of the fit is 0.993. Between $10 M_\odot$ and $1.3 \times 10^3 M_\odot$, bin size variations of $\Delta \log(M/M_\odot)$ between 0.18 and 1.1 result in values of α consistent with 1.7 ± 0.1 . Since α is 1.7, the population is dominated by clumps with low masses, but the total mass is dominated by the most massive clumps; for example, 50% of the population is between 10 and $27 M_\odot$, but contains only 10% of the total mass. The turnover below $\sim 10 M_\odot$ is produced by an incompleteness of the clump catalog caused by the combination of the spatial resolution and flux density limit of the survey. However, observations of higher spatial resolution ($\lesssim 0.01 \text{ pc}$) could result in a spectral mass index of ~ 2.35 , resolving core structures (e.g. Motte et al. 1998). Beltrán et al. (2006) studied a sample of IRAS sources associated with MSFRs in 1.2 mm continuum and found a spectral mass index of 1.5 for clumps with masses between $\sim 10 M_\odot$ and $10^2 M_\odot$ and 2.1 for clumps with masses between $\sim 10^2$ and $10^4 M_\odot$. For clumps identified here with masses higher than $100 M_\odot$, we find a spectral mass index of 1.6 ± 0.1 , as is shown in Fig. 7, in agreement with the previous fit considering clumps with masses between 10 and $1.3 \times 10^3 M_\odot$. It is necessary to observe more whole GMCs to confirm these results.

Clump diameters, D_c , are estimated from the deconvolved FWHM size of their emissions. We used the FWHM size θ_{FWHM}

² <http://www.edpsciences.org>

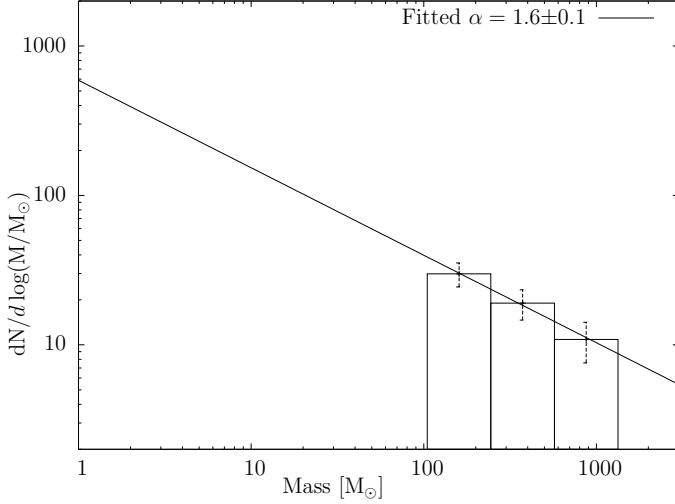


Fig. 7. Mass distribution of identified clumps in G345.5+1.0 with masses higher than $100 M_{\odot}$, plotted as $dN/d\log(M/M_{\odot})$ versus mass, where $dN/d\log(M/M_{\odot})$ is approximated by the number of clumps ΔN within a logarithmic mass interval $\Delta \log(M/M_{\odot})$. Here, $\Delta \log(M/M_{\odot})$ is constant, ~ 0.37 . Error bars are estimated by $\sqrt{\Delta N / \Delta \log(M/M_{\odot})}$. The continuous line represents the mass distribution fit with $dN/d\log(M/M_{\odot}) \propto M^{1-\alpha}$, where the spectral mass index α is 1.6 ± 0.1 for masses between ~ 100 and $1.3 \times 10^3 M_{\odot}$.

estimated by CLUMPFIND algorithm, thus

$$D_c = \sqrt{\theta_{FWHM}^2 - \theta_{beam}^2},$$

where θ_{beam} is the beam-size. Considering a distance of 1.8 kpc to the GMC and clumps that have a reliable D_c , i.e. $D_c \geq \theta_{beam}$, clumps have diameters between 0.2 and 0.6 pc.

From the masses and sizes, and assuming a spherical and homogeneous density distribution, we estimate mean clump densities, using the expression

$$\rho = \mu m_H n,$$

where ρ is the mass density and n is the particle density. Densities of clumps are between 5×10^3 and $4 \times 10^5 \text{ cm}^{-3}$. Mean column densities of clumps, N_c , are estimated as

$$N_c \sim \frac{M_c}{\mu m_H \pi (D_c/2)^2},$$

and range between 4×10^{21} and $4 \times 10^{23} \text{ cm}^{-2}$. Tables 3 and 5 show physical properties for each clump and a summary of them, respectively.

Figure 8 shows a plot of mass versus diameter for the clumps detected toward GMC G345.5+1.0 with reliable diameters. The dotted lines indicate constant densities at 10^3 , 10^4 , 10^5 , and 10^6 cm^{-3} . The majority of clumps have densities between 10^4 and 10^5 cm^{-3} .

The physical properties of detected clumps are similar to those found in other GMCs (e.g. Mookerjee et al. 2004).

4.4. Association with infrared emission (IRAS-MSX-SPITZER)

Stars form in clumps, heating their surrounding dust, which radiates at infrared wavelengths. This is illustrated in Fig. 9 that

Table 3. Summary of the physical properties of the identified clumps.

	$S_{1.2mm}$ Jy	Diameters pc	Masses M_{\odot}	Densities cm^{-3}
Range	0.089-40	0.2-0.6	$3.0-1.3 \times 10^3$	$5 \times 10^3-4 \times 10^5$
Total	3.7×10^2		1.2×10^4	

^a The densities are computed assuming a mean molecular weight of $\mu=2.29$.

shows a strong spatial correlation between the 1.2 mm continuum emission and infrared emission at $21.34 \mu\text{m}$ (from MSX observations). To quantify the correlation, we searched for infrared emission inside clump emission areas, using MSX³ images at 8.28, 12.13, 14.65, and $21.34 \mu\text{m}$ and SPITZER⁴ (IRAC) images at 3.6, 4.5, 5.8, and $8.0 \mu\text{m}$. We find that $\sim 20\%$ of all clumps have an infrared counterpart in all MSX and SPITZER bands (see Table 5). The rest of the clumps, $\sim 80\%$, are not detected in all MSX and SPITZER bands, particularly not in 12.13, 14.65, and $21.34 \mu\text{m}$. Since $8.0 \mu\text{m}$ MSX band and SPITZER IRAC bands are sensitive to the polycyclic aromatic hydrocarbon (PAH) emission and the photospheric emission from stars (e.g. Chavarría et al. 2008), clump not detected in all MSX and SPITZER bands are considered to have no counterpart at infrared wavelengths. Since both the MSX and SPITZER bands have sensitivity limits, the percentage of detections is a lower limit to the number of clumps that are forming stars, and the percentage of failed detections is an upper limit to the number of clumps that are not forming stars.

Nine clumps are associated with six IRAS point sources classified as MSFRs with luminosities $\geq 10^3 L_{\odot}$ (see Sect. 4.5 and Table 4). As Fig. 8 shows, these clumps have densities of $\sim 10^5 \text{ cm}^{-3}$, suggesting that there is a threshold density above which massive stars can form. These values are consistent with the typical density of clumps associated with MSFRs ($\sim 10^5 \text{ cm}^{-3}$; Faúndez et al. 2004).

As Fig. 8 shows, clumps that emit detectable infrared emission tend to be more massive than remaining clumps. Clumps without infrared emission (cold or starless clumps) have a mean mass of $21 M_{\odot}$, and clumps with an infrared counterpart have a mean mass of $2.1 \times 10^2 M_{\odot}$. Furthermore, all clumps with masses higher than $\sim 200 M_{\odot}$ have an infrared counterpart.

MSX point sources associated with clumps within the GMC G345.5+1.0 have mid-infrared colors S_{21}/S_8 from 0.9 to 30, S_{14}/S_8 from 0.4 to 8, and S_{12}/S_8 from 0.7 to 4, where S_8 , S_{12} , S_{14} , and S_{21} are the flux densities at 8.28, 12.13, 14.65, and $21.34 \mu\text{m}$, respectively. These ratios cover those of massive young stellar objects (MYSOs; Lumsden et al. 2002): $S_{21}/S_8 > 2$ and $S_{21} > S_{14} > S_8$. About 7% of the clumps contain MSX sources that satisfy this criterion, and these clumps have masses $\geq 36 M_{\odot}$ (see Fig. 8).

The existence of clumps with and without infrared emission suggests that clumps in the GMC are at different evolutionary stages. Cold clumps have masses between 3.0 and $1.9 \times 10^2 M_{\odot}$, where the most massive ones are possible progenitors of MSFRs. For example, we estimate that the least massive clump associated with a MYSO has a mass of $\sim 36 M_{\odot}$, and we identify seven cold clumps with densities $\geq 10^5 \text{ cm}^{-3}$ and masses $\geq 36 M_{\odot}$, which will eventually collapse to form high-mass stars.

³ <http://irsa.ipac.caltech.edu/>

⁴ <http://irsa.ipac.caltech.edu/>

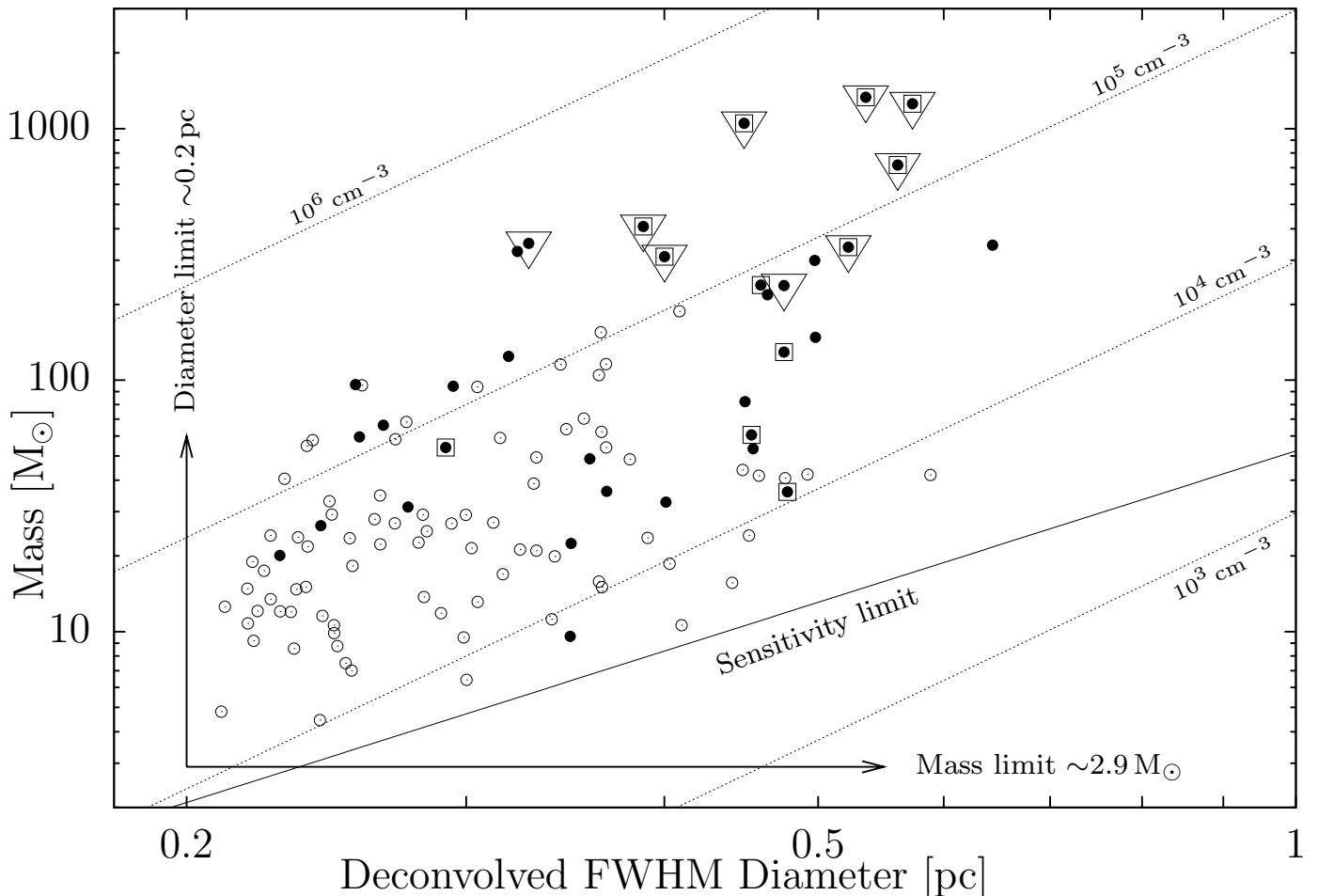


Fig. 8. Mass versus diameter for the clumps detected toward the GMC G345.5+1.0 in 1.2 mm continuum emission with reliable diameters. Filled circles indicate clumps detected in infrared MSX and SPITZER bands. Open circles indicate clumps that do not have an infrared counterpart. Triangles indicate clumps associated with MSFR-IRAS sources, which have luminosities $>10^3 L_{\odot}$. Boxes indicate clumps associated with MSX sources that satisfy MYSO candidate criterion (Lumsden et al. 2002). Arrows mark detection limits for masses ($\sim 2.9 M_{\odot}$) and diameters (~ 0.2 pc). The continuous line indicates the detectable mass as a function of diameter (sensitivity limit), considering an intensity limit of five rms (~ 0.1 Jy beam $^{-1}$). Dotted lines indicate mean densities at 10^3 , 10^4 , 10^5 and 10^6 cm $^{-3}$. The densities are computed assuming a mean molecular weight of $\mu=2.29$.

Do clumps form single stars? One way to assess this is to compare the slope of the clump mass distribution with that of the stellar initial mass function (IMF) (e.g. Motte et al. 1998; Lada et al. 2007). Equal slopes would indicate that the origin of the stellar IMF has its direct roots in the origin of the clump mass distribution. The spectral mass index α of the clump mass distribution determined here is consistent with that of other investigations (e.g. Muñoz et al. 2007), but differs from that estimated for the stellar IMF of the solar neighborhood for stellar masses higher than $0.5 M_{\odot}$ ($\alpha \sim 2.35$; e.g. Kroupa 2002). This suggests that the detected clumps do not directly form stars, and other processes are necessary to determine the stellar initial masses, such as the fragmentation of clumps, mainly of the most massive ones. Figure 6 compares the IMF spectral mass index with the clump mass distribution.

4.5. Dust properties of massive-star forming regions associated with clumps and IRAS point sources

Regions of massive star formation are embedded in massive clumps, and the intense Lyman flux produced by them heats the surrounding dust, which re-emits mainly at far infrared wavelengths with characteristic colors. To study the physical properties of dust in these regions, we examine the spectral energy distributions (SEDs) of MSFRs associated with IRAS point sources and clumps detected here, assuming that their emissions are from dust.

Within the GMC, there are eight MSFRs associated with IRAS-CS sources (Table 2). We added one more source, IRAS 16533-4009, which is embedded in 1.2 mm continuum emission, has a high luminosity, $\sim 9 \times 10^4 L_{\odot}$, and increasing IRAS flux densities from 12 to $100 \mu\text{m}$; however it does not satisfy the far-infrared color criterion defined by Wood & Churchwell (1989), since its flux density in $25 \mu\text{m}$ is an upper limit. Figure 11 shows $8.0 \mu\text{m}$ images from SPITZER data with contours of 1.2 mm continuum emission for all these sources. For six of these objects, the SPITZER emission is embedded within

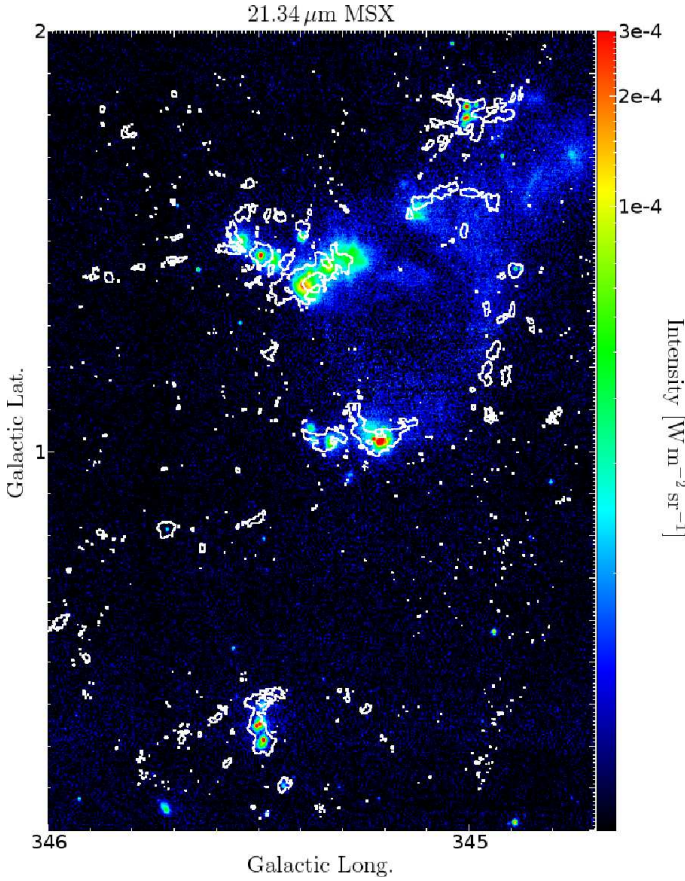


Fig. 9. Image in $21.34\mu\text{m}$ from MSX observations toward GMC G345.5+1.0 with contours of 1.2 mm continuum emission at three times rms, $\sim 0.06\text{Jy beam}^{-1}$.

1.2 mm continuum emission. For more reliable estimates in our SED study, we only consider these six sources: IRAS 16533-4009, IRAS 16562-3959, IRAS 16571-4029, IRAS 16596-4012, IRAS 17008-4040, and IRAS 17009-4042.

Figure 12 displays the six SEDs constructed using our observations in 1.2 mm continuum emission, infrared data at 12, 25, 60, and $100\mu\text{m}$ from the IRAS Point Source Catalog (version 2.0), and at 8.3, 12.1, 14.7 and $21.3\mu\text{m}$ from the MSX Point Source Catalog (version 2.3). Because observations were performed using different beam sizes, for IRAS $\sim 300''$, for MSX $\sim 20''$, and for 1.2 mm $24''$, we consider all emission within the IRAS beam; thus, two SEDs are associated with more than one 1.2 mm clump.

The SEDs of MSFRs can be modeled as several dust components at different temperatures (e.g. Faúndez et al. 2004; Morales et al. 2009). Because of the shape of the six SEDs, we model them as two dust components at different temperatures, cold and warm components, including the absorption of the radiation by assuming that the warm component is embedded in the cold one. The total flux density, S_ν^{total} , at frequency ν is approximated by

$$S_\nu^{\text{total}} \sim S_\nu^{\text{cold}} + S_\nu^{\text{warm}},$$

where

$$S_\nu^{\text{cold}} = \Omega^{\text{cold}} B_\nu(T_{\text{dust}}^{\text{cold}}) (1 - \exp(-\tau_\nu^{\text{cold}}))$$

and

$$S_\nu^{\text{warm}} = \Omega^{\text{warm}} B_\nu(T_{\text{dust}}^{\text{warm}}) (1 - \exp(-\tau_\nu^{\text{warm}})) \exp(-\tau_\nu^{\text{cold}}/2).$$

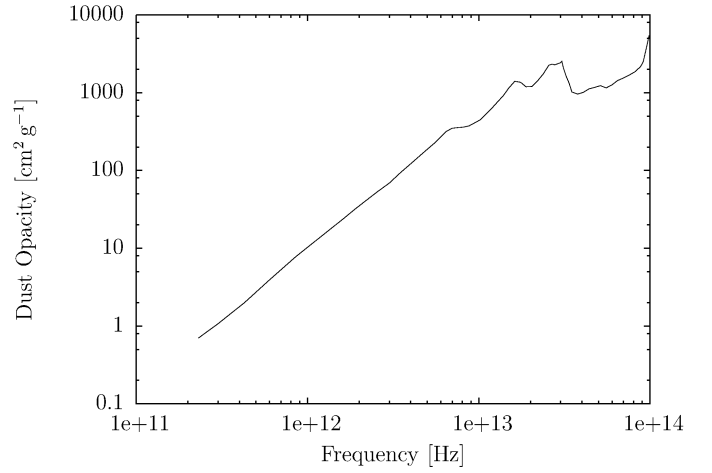


Fig. 10. Dust opacity spectrum utilized in the SED models. It was estimated by Ossenkopf & Henning (1994)^a, assuming a Mathis-Rumpl-Nordsieck initial size distribution with thin ice mantles and 10^5 yr of coagulation at a gas density of 10^5cm^{-3} .

^a <http://vizier.u-strasbg.fr/viz-bin/VizieR, J/A+A/291/943/table1>

The parameters S_ν^{cold} , Ω^{cold} , $T_{\text{dust}}^{\text{cold}}$, and τ_ν^{cold} are the flux density, the solid angle, the dust temperature, and the optical depth of the cold component, respectively, and S_ν^{warm} , Ω^{warm} , $T_{\text{dust}}^{\text{warm}}$, and τ_ν^{warm} are the flux density, the solid angle, the dust temperature, and the optical depth of the warm component, respectively. In addition, $B_\nu(T_{\text{dust}}^{\text{cold}})$ and $B_\nu(T_{\text{dust}}^{\text{warm}})$ are the Planck function at dust temperatures $T_{\text{dust}}^{\text{cold}}$ and $T_{\text{dust}}^{\text{warm}}$, respectively. For both components, Ω can be expressed as

$$\Omega = \pi (\theta/2)^2,$$

where θ is the angular diameter. The optical depths are given by (e.g. Evans 1999)

$$\tau_\nu^{\text{cold}} = N_{\text{dust}}^{\text{cold}} k_\nu \quad \text{and} \quad \tau_\nu^{\text{warm}} = N_{\text{dust}}^{\text{warm}} k_\nu,$$

where $N_{\text{dust}}^{\text{cold}}$ and $N_{\text{dust}}^{\text{warm}}$ are the dust column densities in g cm^{-2} for the cold and warm components, and k_ν is the dust opacity. We use dust opacities estimated by Ossenkopf & Henning (1994) for protostellar cores. They computed opacities considering the Mathis-Rumpl-Nordsieck (MRN) distribution for the diffuse interstellar medium (Draine & Lee 1984) as the initial size distribution for dust, without and with ice (thin and thick), and without and with coagulation (after 10^5 years for densities between 10^5 - 10^8cm^{-3}). In the case of regions with ice depletion produced by the heating of central sources, they recommended opacities for the model with thin ice mantles and coagulation for a density of 10^5cm^{-3} . These dust opacities are shown in Fig. 10, for frequencies between $\sim 2.3 \times 10^{11}$ and 10^{14}Hz .

Thus, in our SED model, each dust component has three values to fit of T_{dust} , θ , and N_{dust} . However, the dust column density of the warm component, $N_{\text{dust}}^{\text{warm}}$, is difficult to estimate, because it is more sensitive to the emission in the Rayleigh-Jeans part of the spectrum ($h\nu \ll kT_{\text{warm}}$), where the emission is dominated by the cold component. To overcome this problem, we assume that the two components have equal densities, thus

$$N_{\text{dust}}^{\text{warm}} \sim \frac{\theta_{\text{dust}}^{\text{warm}}}{\theta_{\text{dust}}^{\text{cold}}} N_{\text{dust}}^{\text{cold}}.$$

Given the simplicity of the SED model and the poor sensitivity of the data to $N_{\text{dust}}^{\text{warm}}$, a more realistic density distribution is unnecessary.

To enable a more reliable comparison, angular diameters are converted into spatial diameters, and dust column densities to gas column densities. Thus

$$D_{\text{dust}}^{\text{cold}} = d \theta_{\text{dust}}^{\text{cold}},$$

$$D_{\text{dust}}^{\text{hot}} = d \theta_{\text{dust}}^{\text{warm}},$$

and

$$N_{\text{gas}}^{\text{cold}} = \frac{N_{\text{dust}}^{\text{cold}} R_{\text{gd}}}{\mu m_{\text{H}}},$$

where $\theta_{\text{dust}}^{\text{cold}}$ and $\theta_{\text{dust}}^{\text{warm}}$ are in radians. In this way, our model has five variables: dust temperatures and sizes for the two components, and gas column density for the cold component.

Table 4 and Fig. 12 display the results of the fits. The mean dust temperatures of each component are 28 ± 5 K (cold) and 200 ± 10 K (warm). The sizes and column densities of the cold component agree with those estimated by 1.2 mm continuum: sizes vary by a factor of 0.7-1.5 and column densities vary by a factor of 0.5-3. Estimates of luminosities, from the integration of SED models, are $> 10^3 L_{\odot}$. Given the sizes and column densities, the total mass is dominated by the cold component ($\sim 99\%$ of the total mass), and is similar to that estimated from the 1.2 mm continuum emission, varying by a factor of 0.8-1.6.

Dust characteristics of clumps associated with MSFRs estimated in this paper are consistent with previous works (e.g. Faúndez et al. 2004; Molinari et al. 2000; Molinari et al. 2008), where the cold dust temperature in regions of massive star formation is ~ 30 K.

The SED models have a discrepancy with data in $\sim 12 \mu\text{m}$ bands (see Fig. 12), which can be produced by not considering the PAH emission in the SED models (e.g. van Dishoeck 2004), or by an excess in the dust opacities utilized at these wavelengths, affecting the modeled radiation from the hot component that is absorbed by the cold one.

The dependence of SED models on variations in the fitted parameters is shown in Fig. 13, which displays the SED for clump 1, or IRAS 16562-3959, with the best-fit model and models with variations in the fitted parameters $T_{\text{dust}}^{\text{cold}}$, $D_{\text{dust}}^{\text{cold}}$, $T_{\text{dust}}^{\text{warm}}$, $D_{\text{dust}}^{\text{warm}}$, and $N_{\text{gas}}^{\text{cold}}$. For each dust component, variations in its temperature affect both its peak emission frequency and its luminosity, both values increasing as the temperature increases. Variations in either $D_{\text{dust}}^{\text{cold}}$ or $N_{\text{gas}}^{\text{cold}}$ affect the luminosities of the two components; when $D_{\text{dust}}^{\text{cold}}$ or $N_{\text{gas}}^{\text{cold}}$ increases, the luminosity of the cold dust component increases, whereas radiation absorption of the warm component also increases, reducing its luminosity. When $D_{\text{dust}}^{\text{warm}}$ increases, the luminosity also increases.

5. Conclusions

We have robustly detected the whole of the GMC G345.5+1.0 in 1.2 mm continuum emission at a spatial resolution of 0.2 pc, and conclude that:

- The GMC is fragmented. We have identified 201 clumps, which have beam-corrected diameters between 0.2 and 0.6 pc, masses between 3.0 and $1.3 \times 10^3 M_{\odot}$, and densities between 5×10^3 and $4 \times 10^5 \text{ cm}^{-3}$.
- The total mass of the clumps is $\sim 1.2 \times 10^4 M_{\odot}$, and after comparing with the total mass of the GMC of $\sim 6.5 \times 10^5 M_{\odot}$, we inferred that the efficiency in forming these clumps is ~ 0.02 .

- The clump mass distribution is well-fitted by a power law $dN/dM \propto M^{-\alpha}$, where the spectral mass index α is 1.7 ± 0.1 . The total mass is dominated by massive clumps, but the population is dominated by clumps with low masses.
- The spectral mass index of the clump mass distribution is different from that of the stellar IMF. Thus our detected clumps are probably not the direct progenitors of single stars.
- Comparing with MSX and SPITZER (IRAC-bands) observations, 20% of the clumps have an infrared counterpart in all MSX and SPITZER bands. The remaining clumps, $\sim 80\%$, are considered to have no counterpart at infrared wavelengths. The percentage of detection is a lower limit to the number of clumps forming stars, while the percentage of no detections is an upper limit to the number of clumps that are not forming stars.
- Regions of massive-star formation within the cloud, associated with IRAS point sources, have SEDs that can be modeled with two dust components at different mean temperatures of 28 ± 5 and 200 ± 10 K.

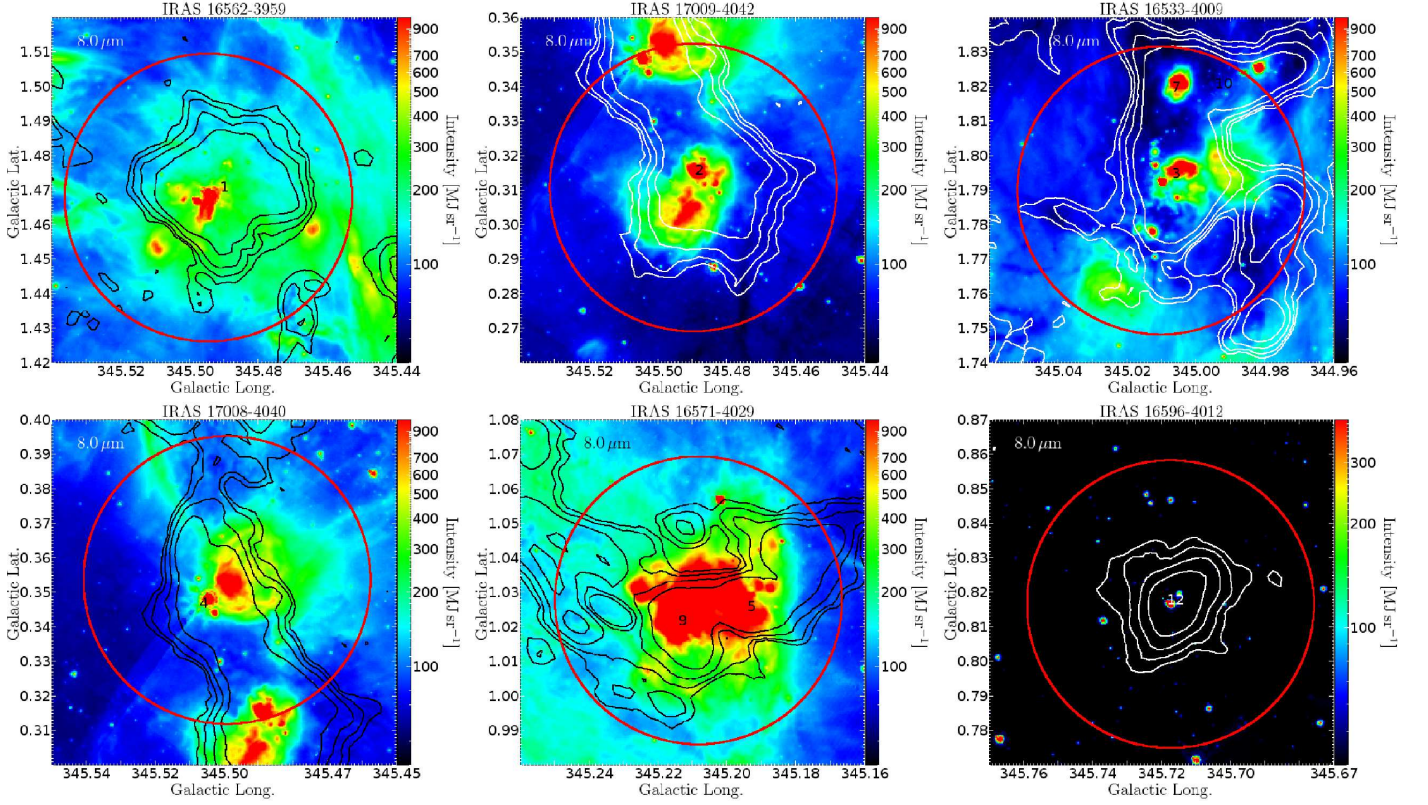
Acknowledgements. C.L. acknowledges partial support from the GEMINI-CONICYT FUND, project number 32070020, and ESO-University of Chile Student Fellowship. This work was supported by the Chilean Center for Astrophysics FONDAF N° 15010003 and by Center of Excellence in Astrophysics and Associated Technologies PFB 06.

References

- Alvarez, H., May, J., & Bronfman, L. 1990, *ApJ*, 348, 495.
 Bains, I., Wong, T., Cunningham, M. et al. 2006, *MNRAS*, 367, 1609.
 Ballesteros-Paredes, J., Gazol, A., Kim, J. et al. 2006, *ApJ*, 637, 384.
 Ballesteros-Paredes, J., Klessen, R. S., Mac Low, M.-M. & Vázquez-Semadeni, E. 2007, *Protostars and Planets V*, p. 63. Edited by Reipurth, B., Jewitt, D. & Keil, K. Published by University of Arizona Press.
 Beltrán, M. T., Brand, J., Cesaroni, R. et al. 2006, *A&A*, 447, 221.
 Bohlin, R. C., Savage, B. D., & Drake, J. F. 1978, *ApJ*, 224, 132.
 Bonnell, I. A., Larson, R. B., & Zinnecker, H. 2007, *Protostars and Planets V*, p. 149. Edited by Reipurth, B., Jewitt, D. & Keil, K. Published by University of Arizona Press.
 Bronfman, L., Alvarez, H., Cohen, R. S., & Thaddeus, P. 1989, *ApJ*, 71, 481.
 Bronfman, L., Nyman, L.-Å., & May, J. 1996, *A&A*, 115, 81.
 Bronfman, L., Casassus, S., May, J., & Nyman, L.-Å. 2000, *A&A*, 358, 521.
 Chavarría, L. A., Allen, L. E., Hora, J. L., Brunt, C. M., & Fazio, G. G. 2008, *ApJ*, 682, 445.
 Dame, T. M., Elmegreen, B. G., Cohen, R. S., & Thaddeus, P. 1986, *ApJ*, 305, 892.
 Draine, B. T., & Lee, H. M. 1984, *ApJ*, 285, 89.
 Evans, N. J. 1999, *ARA&A*, 37, 311.
 Faúndez, S., Bronfman, L., Garay, G. et al. 2004, *A&A*, 426, 97.
 Garay, G., Faúndez, S., Mardones, D. et al. 2004, *ApJ*, 610, 313.
 Grabelsky, D. A., Cohen, R. S., Bronfman, L., & Thaddeus, P. 1988, *ApJ*, 331, 181.
 Hildebrand, R. H. 1983, *QJRAS*, 24, 267.
 Hill, T., Burton, M. G., Minier, V. et al. 2005, *MNRAS*, 363, 405.
 Hunter, S. D., Bertsch, D. L., Catelli, J. R. et al. 1997, *ApJ*, 481, 205.
 Klessen, R. S., Burkert, A., & Bate, M. R. 1998, *ApJ*, 501, 205.
 Kroupa, P. 2002, *Science*, 295, 82.
 Lada, C. J., Alves, J. F., & Lombardi, M. 2007, *Protostars and Planets V*, p. 3. Edited by Reipurth, B., Jewitt, D. & Keil, K. Published by University of Arizona Press.
 Li, Y., Mac Low, M.-M., & Klessen, R. S. 2005, *ApJ*, 626, 823.
 Lumsden, S. L., Hoare, M. G., Oudmaier, R. D., & Richards, D. 2002, *MNRAS*, 336, 621.
 Molinari, S., Brand, J., Cesaroni, R., & Palla, F. 2000, *A&A*, 355, 617.
 Molinari, S., Pezzuto, S., Cesaroni, R. et al. 2008, *A&A*, 481, 345.
 Mookerjee, B., Kramer, C., Nielbock, M., & Nyman, L.-Å. 2004, *A&A*, 426, 119.
 Morales, E. F. E., Mardones, D., Garay, G. et al. 2009, *ApJ*, 698, 488.

- Motte, F., André, P., & Neri, R. 1998, *A&A*, 336, 150.
- Motte, F., Bontemps, S., Schilke, P. et al. 2007, *A&A*, 476, 1243.
- Muñoz, D.J., Mardones, D., Garay, G., & Rebolledo, D. 2007, *ApJ*, 668, 906.
- Ossenkopf, V., & Henning, Th. 1994, *A&A*, 291, 943.
- Panagia, N. 1973, *ApJ*, 78, 929.
- Sanders, D. B., Scoville, N. Z., & Solomon, P. M. 1985, *ApJ*, 289, 373.
- Solomon, P. M., Rivolo, A. R., Barrett, J., & Yahil, A. 1987, *ApJ*, 319, 730.
- Williams, J. P., De Geus, E. J., & Blitz, L. 1994, *ApJ*, 428, 693.
- Williams, J. P., & McKee, C. F. 1997, *ApJ*, 476, 166.
- Williams, J. P., Blitz, L., & McKee, C. F. 2000, *Protostars and Planets IV*, p 97. Edited by Mannings, V., Boss, A. P., & Russell, S. S. Published by University of Arizona Press.
- Wood, D. O. S., & Churchwell, E. 1989, *ApJ*, 340, 265.
- van Dishoeck 2004, *ARA&A*, 42, 119.
- Zinnecker, H. & York, H. 2007, *ARA&A*, 45, 481.

Embedded sources



Partially embedded sources

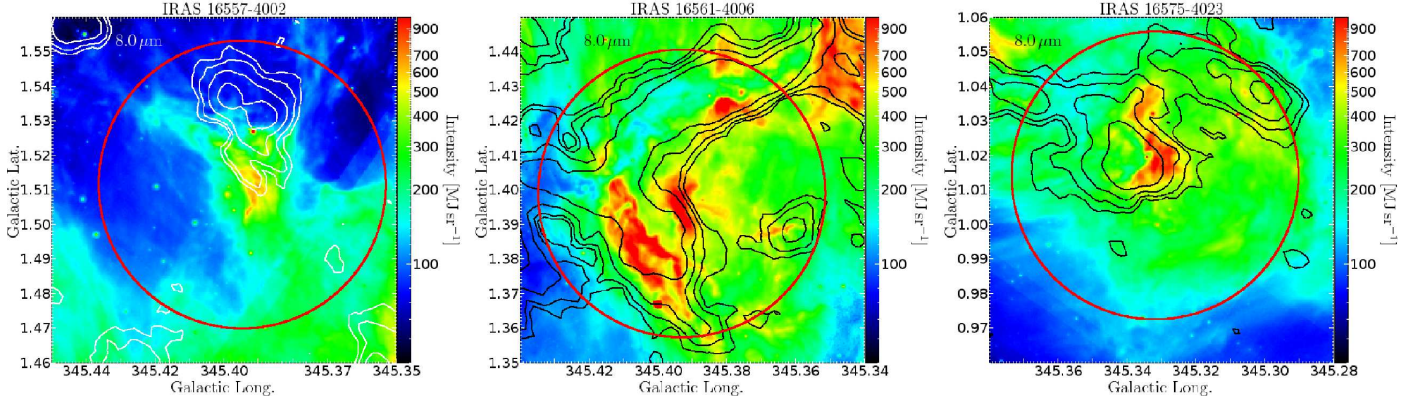


Fig. 11. Images of $8.0\mu\text{m}$ emission (SPITZER data) toward clumps detected in 1.2 mm continuum emission and associated with IRAS point sources. Contours represent 1.2 mm continuum emission at $0.06, 0.12, 0.24,$ and 0.48 Jy beam^{-1} (rms is 0.02 Jy beam^{-1}). IRAS source names are given at the top of each image, and clump numbers are indicated at the peak of 1.2 mm continuum emission. Red circles are centered on the coordinates of IRAS point sources, with diameters of $5'$ (an approximation of the angular resolution of IRAS observations at $100\mu\text{m}$).

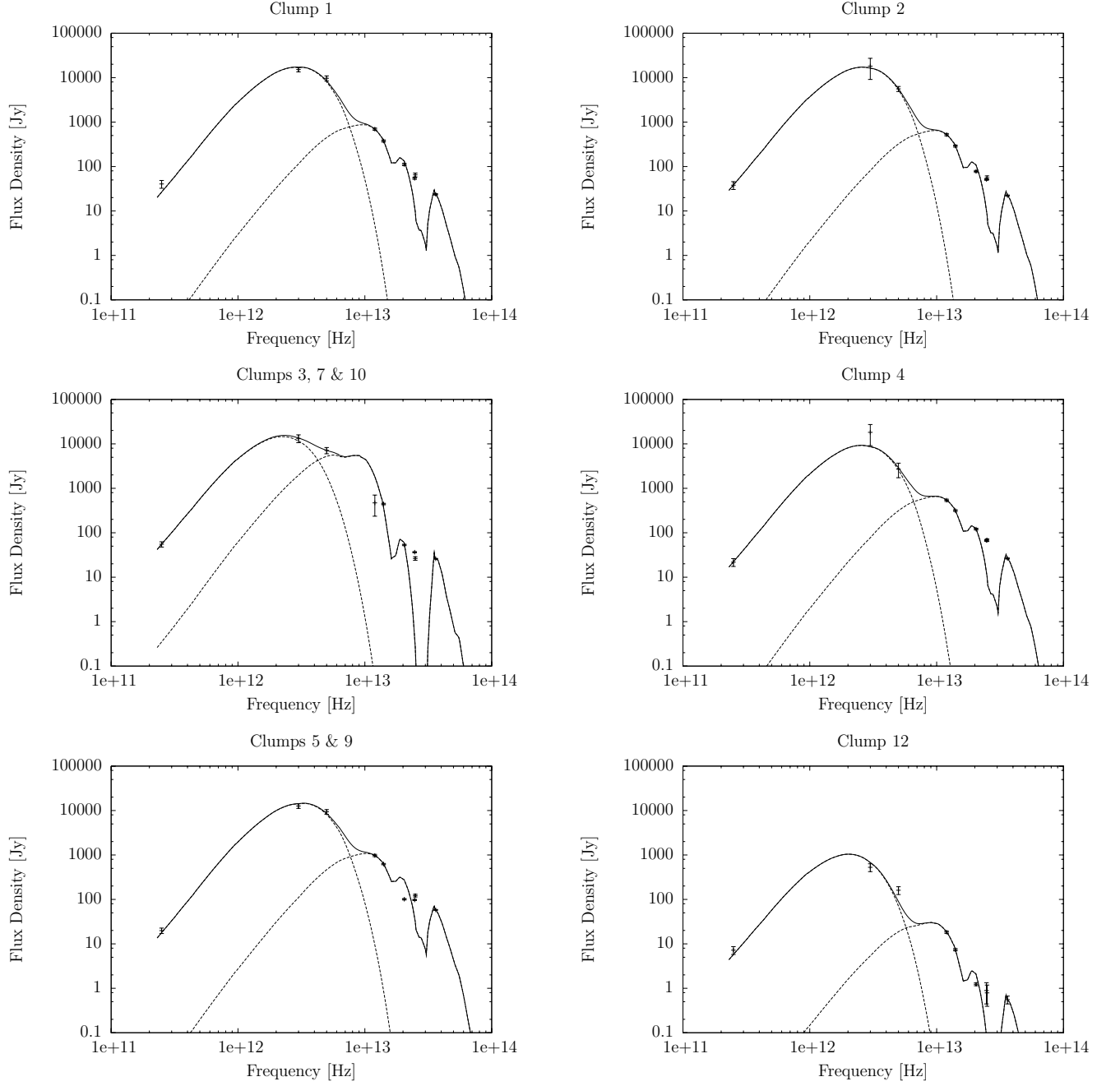


Fig. 12. The SEDs of massive-star forming regions associated with massive clumps detected in 1.2 mm continuum emission; top labels show names of the clumps. Dots with error bars are flux densities estimated from SIMBA, IRAS, and MSX observations. Each SED is modeled with two dust components at different temperatures (physical parameters for each model are in Table 4); drawn lines are the total flux density of the two dust components, and dashed lines are the contributions of each dust component.

Table 4. SED models for MSFRs associated with IRAS point sources and massive clumps detected in 1.2 mm continuum emission. Each model consists of two dust components with equal densities at different temperatures (cold and warm components). Column 1 shows names of IRAS point sources; Column 2, names of clumps; in Columns 3 to 8, we show the fitted physical parameters: dust temperature, diameter, and column density, respectively, for the cold (Cols. 3-5) and warm (Cols. 6-8) components; Column 9, masses of the cold component; and Column 10, total luminosities.

IRAS	Clumps	Cold			Warm			Cold mass $10^3 M_{\odot}$	Luminosity $10^4 L_{\odot}$
		T_{dust} K	D_{dust} pc	N_{gas} 10^{23} cm^{-2}	T_{dust} K	D_{dust} pc	N_{gas} 10^{22} cm^{-2}		
16562-3959	1	32	0.67	1.6	194	0.03	0.69	1.0	5.3
17009-4042	2	29	0.86	1.6	202	0.03	0.51	1.7	4.7
16533-4009	3, 7, 10	25	0.79	3.2	205	0.07	2.7	2.8	9.4
17008-4040	4	28	0.68	1.5	205	0.03	0.57	1.0	2.9
16571-4029	5, 9	34	0.58	1.3	209	0.03	0.65	0.64	5.3
16596-4012	12	22	0.34	2.2	203	0.008	0.49	0.36	0.22

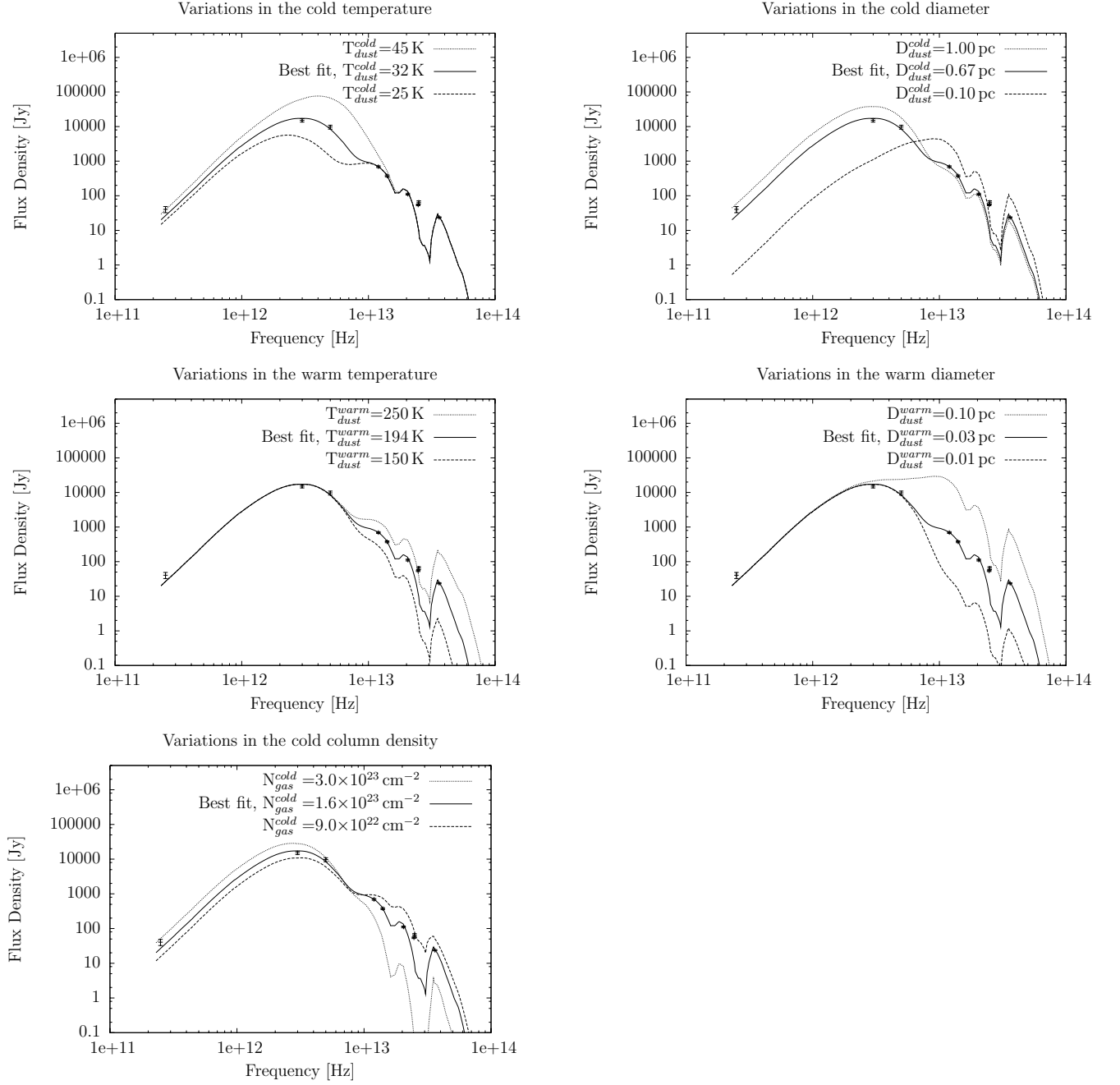


Fig. 13. Dependence of the SED model on variations in the fitted parameters. Plots show the SED for clump 1 with the best-fit model (see Table 4) and variations in each parameter, for T_{dust}^{cold} , D_{dust}^{cold} , T_{dust}^{warm} , D_{dust}^{warm} and N_{gas}^{cold} , when increasing and decreasing the best-fit value.

Table 5. Properties of identified clumps in the GMC G345.5+1.0. Column 1 gives clump names; columns 2 and 3, Galactic coordinates of peaks in 1.2 mm continuum emission; column 4, 1.2 mm flux densities; column 5, diameters; column 6, masses; column 7, densities; column 8, column densities; and column 9, if clumps are detected in all infrared MSX and SPITZER-IRAC bands (“Y”) or not (“N”). The densities and the column densities are computed assuming a mean molecular weight of $\mu=2.29$.

Name	Galactic coord. long.	lat.	$S_{1.2mm}$ Jy	Diameter pc	Mass M_{\odot}	Density cm^{-3}	Column density cm^{-2}	Infrared counterpart
1	345.490	1.471	40	0.5	1.3×10^3	2.9×10^5	3.2×10^{23}	Y
2	345.488	0.316	38	0.6	1.3×10^3	2.3×10^5	2.7×10^{23}	Y
3	345.006	1.795	32	0.5	1.1×10^3	3.9×10^5	3.6×10^{23}	Y
4	345.506	0.347	22	0.6	7.2×10^2	1.4×10^5	1.6×10^{23}	Y
5	345.193	1.026	11	0.3	3.5×10^2	3.3×10^5	2.3×10^{23}	Y
6	345.385	1.428	9.8	0.3	3.3×10^2	3.3×10^5	2.2×10^{23}	Y
7	345.006	1.820	12	0.4	4.1×10^2	2.4×10^5	1.9×10^{23}	Y
8	345.179	1.043	9.1	0.5	3.0×10^2	8.2×10^4	8.4×10^{22}	Y
9	345.213	1.022	9.4	0.4	3.1×10^2	1.6×10^5	1.3×10^{23}	Y
10	344.992	1.821	10	0.5	3.4×10^2	8.0×10^4	8.6×10^{22}	Y
11	345.115	1.592	6.6	0.5	2.2×10^2	7.4×10^4	7.0×10^{22}	Y
12	345.716	0.818	7.2	0.5	2.4×10^2	7.5×10^4	7.3×10^{22}	Y
13	345.337	1.018	7.2	0.5	2.4×10^2	8.3×10^4	7.8×10^{22}	Y
14	344.976	1.783	5.7	0.4	1.9×10^2	9.3×10^4	7.8×10^{22}	N
15	344.980	1.752	3.5	0.3	1.2×10^2	9.6×10^4	6.8×10^{22}	N
16	345.367	1.434	3.8	0.3	1.2×10^2	1.3×10^5	8.5×10^{22}	Y
17	345.296	1.452	10	0.6	3.4×10^2	4.4×10^4	5.8×10^{22}	Y
18	345.401	1.419	4.7	0.4	1.6×10^2	1.1×10^5	8.1×10^{22}	N
19	345.418	1.401	2.9	0.3	95	1.9×10^5	1.0×10^{23}	N
20	345.395	1.380	4.5	0.5	1.5×10^2	4.0×10^4	4.1×10^{22}	Y
21	345.411	1.406	2.9	0.3	96	1.9×10^5	1.0×10^{23}	Y
22	345.434	1.405	2.8	0.3	94	1.1×10^5	7.0×10^{22}	N
23	345.443	1.387	3.5	0.4	1.2×10^2	7.9×10^4	6.0×10^{22}	N
24	345.453	1.386	3.2	0.4	1.1×10^2	7.4×10^4	5.5×10^{22}	N
25	345.406	1.394	2.9	0.3	95	1.3×10^5	7.6×10^{22}	Y
26	345.389	1.531	2.0	0.3	66	1.2×10^5	6.5×10^{22}	Y
27	345.554	1.508	1.7	0.2	58	1.4×10^5	7.0×10^{22}	N
28	345.398	1.538	1.7	0.2	55	1.4×10^5	6.7×10^{22}	N
29	345.244	1.021	1.8	0.3	58	9.9×10^4	5.5×10^{22}	N
30	345.301	1.040	1.8	0.3	60	1.2×10^5	6.3×10^{22}	Y
31	345.525	1.567	1.8	0.3	59	6.4×10^4	4.1×10^{22}	N
32	345.396	1.389	1.5	–	49	–	–	Y
33	345.251	1.038	2.1	0.3	68	1.1×10^5	6.3×10^{22}	N
34	344.878	1.437	3.9	0.5	1.3×10^2	4.1×10^4	4.0×10^{22}	Y
35	345.353	1.448	2.5	0.5	82	3.1×10^4	2.8×10^{22}	Y
36	345.236	1.040	2.1	0.4	70	5.3×10^4	3.9×10^{22}	N
37	344.946	1.796	1.6	0.4	54	3.7×10^4	2.8×10^{22}	N
38	345.442	1.558	1.2	0.2	41	1.1×10^5	5.3×10^{22}	N
39	345.257	1.073	1.6	0.3	54	7.4×10^4	4.4×10^{22}	Y
40	345.368	1.036	1.6	0.5	53	1.9×10^4	1.8×10^{22}	Y
41	344.942	1.241	0.55	–	18	–	–	N
42	345.539	1.567	1.5	0.3	49	4.5×10^4	3.1×10^{22}	N
43	345.254	1.052	1.9	0.4	64	5.2×10^4	3.7×10^{22}	N
44	344.904	1.803	1.9	0.4	62	4.3×10^4	3.3×10^{22}	N
45	345.502	0.842	0.88	0.3	29	4.4×10^4	2.6×10^{22}	N
46	345.559	1.531	0.85	0.3	28	5.2×10^4	2.8×10^{22}	N

Continued on next page

Table 5 – continued from previous page

Name	Galactic coord. long.	lat.	$S_{1.2mm}$ Jy	Diameter pc	Mass M_{\odot}	Density cm^{-3}	Column density cm^{-2}	Infrared counterpart
47	345.360	1.389	0.80	0.2	26	6.2×10^4	3.1×10^{22}	Y
48	345.441	0.206	1.8	0.5	61	2.2×10^4	2.0×10^{22}	Y
49	345.137	1.564	0.61	0.2	20	5.7×10^4	2.7×10^{22}	Y
50	345.312	1.046	0.95	0.3	31	5.0×10^4	2.9×10^{22}	Y
51	345.445	1.371	1.3	0.5	42	1.5×10^4	1.4×10^{22}	N
52	345.334	1.428	1.5	0.4	49	3.6×10^4	2.6×10^{22}	Y
53	345.563	1.486	1.1	0.3	35	6.3×10^4	3.5×10^{22}	N
54	344.929	1.836	0.50	–	17	–	–	N
55	345.335	1.434	1.1	0.5	36	1.1×10^4	1.1×10^{22}	Y
56	345.434	1.445	1.00	0.3	33	7.5×10^4	3.8×10^{22}	N
57	345.211	1.049	0.55	0.3	18	3.7×10^4	2.0×10^{22}	N
58	345.968	0.598	1.5	0.4	49	3.0×10^4	2.3×10^{22}	N
59	344.945	1.229	0.43	–	14	–	–	N
60	345.006	1.532	1.1	0.4	36	2.5×10^4	1.9×10^{22}	Y
61	345.265	1.085	1.2	0.3	39	3.6×10^4	2.5×10^{22}	N
62	344.952	1.195	0.88	0.3	29	6.6×10^4	3.3×10^{22}	N
63	345.337	1.037	0.99	0.4	33	1.7×10^4	1.4×10^{22}	Y
64	345.436	1.418	0.67	0.3	22	4.0×10^4	2.2×10^{22}	N
65	345.501	0.418	0.66	0.2	22	5.4×10^4	2.7×10^{22}	N
66	345.457	0.428	0.81	0.3	27	3.6×10^4	2.2×10^{22}	N
67	344.933	1.251	0.73	0.2	24	7.1×10^4	3.3×10^{22}	N
68	345.064	1.747	0.57	0.2	19	6.0×10^4	2.7×10^{22}	N
69	345.501	0.389	1.3	0.5	42	1.2×10^4	1.2×10^{22}	N
70	345.468	1.431	0.33	–	11	–	–	Y
71	345.558	1.522	0.40	–	13	–	–	N
72	345.010	1.764	0.60	0.3	20	1.7×10^4	1.2×10^{22}	N
73	345.590	1.491	0.19	–	6.2	–	–	N
74	344.932	1.231	0.23	–	7.5	–	–	N
75	344.927	1.806	0.82	0.3	27	3.0×10^4	1.9×10^{22}	N
76	344.947	1.813	0.48	0.4	16	1.1×10^4	8.3×10^{21}	N
77	344.955	1.170	0.72	0.2	24	6.2×10^4	3.0×10^{22}	N
78	344.936	1.245	0.30	–	10	–	–	N
79	345.384	1.038	0.68	0.3	23	3.5×10^4	2.0×10^{22}	N
80	345.548	1.480	0.34	–	11	–	–	Y
81	345.513	0.407	0.82	0.3	27	4.6×10^4	2.6×10^{22}	N
82	345.563	1.526	0.36	0.2	12	3.2×10^4	1.5×10^{22}	N
83	345.450	1.364	0.34	–	11	–	–	N
84	345.429	1.455	0.88	0.3	29	3.7×10^4	2.3×10^{22}	N
85	345.010	1.617	0.45	–	15	–	–	N
86	345.001	1.615	1.2	0.5	41	1.3×10^4	1.3×10^{22}	N
87	345.319	1.484	0.68	0.4	22	1.8×10^4	1.3×10^{22}	Y
88	345.519	1.639	0.71	0.3	24	4.9×10^4	2.5×10^{22}	N
89	345.133	1.069	1.3	0.6	42	7.0×10^3	8.4×10^{21}	N
90	345.396	1.519	0.42	–	14	–	–	Y
91	345.033	1.632	0.76	0.3	25	3.7×10^4	2.2×10^{22}	N
92	345.476	1.568	0.31	–	10	–	–	N
93	344.966	1.181	0.41	–	14	–	–	N
94	345.240	0.390	0.49	–	16	–	–	N
95	345.524	0.404	0.46	0.2	15	3.8×10^4	1.9×10^{22}	N
96	345.590	0.374	0.40	–	13	–	–	Y
97	345.031	1.781	0.56	0.4	19	9.6×10^3	8.0×10^{21}	N
98	345.451	0.435	0.39	–	13	–	–	N
99	345.078	1.786	0.64	0.3	21	1.9×10^4	1.3×10^{22}	N
100	345.854	1.415	0.47	–	16	–	–	N

Continued on next page

Table 5 – continued from previous page

Name	Galactic coord. long.	lat.	$S_{1.2mm}$ Jy	Diameter pc	Mass M_{\odot}	Density cm^{-3}	Column density cm^{-2}	Infrared counterpart
101	345.217	0.999	0.51	0.3	17	1.8×10^4	1.2×10^{22}	N
102	344.936	1.596	0.44	–	15	–	–	N
103	345.065	1.615	1.3	0.5	44	1.7×10^4	1.5×10^{22}	N
104	345.338	1.463	0.73	0.5	24	8.8×10^3	8.2×10^{21}	N
105	345.585	1.484	0.41	0.2	14	3.9×10^4	1.8×10^{22}	N
106	345.854	1.421	0.29	–	9.5	–	–	N
107	345.062	1.842	0.53	0.2	18	5.3×10^4	2.4×10^{22}	N
108	345.477	1.563	0.22	–	7.2	–	–	N
109	345.454	1.358	0.16	–	5.4	–	–	N
110	345.959	0.608	0.33	–	11	–	–	N
111	344.949	1.213	0.27	–	8.8	–	–	N
112	344.942	1.589	0.45	–	15	–	–	N
113	345.539	1.488	0.29	0.3	9.5	1.2×10^4	7.4×10^{21}	N
114	345.576	0.258	0.26	–	8.5	–	–	N
115	345.681	0.318	0.43	–	14	–	–	N
116	345.330	1.049	0.45	0.2	15	3.9×10^4	1.9×10^{22}	N
117	345.776	1.445	0.34	–	11	–	–	N
118	345.511	1.578	0.40	0.3	13	1.6×10^4	9.8×10^{21}	N
119	344.909	1.182	0.65	0.3	22	2.6×10^4	1.6×10^{22}	N
120	345.518	0.835	0.34	–	11	–	–	N
121	345.873	0.811	0.30	–	10	–	–	N
122	345.489	0.430	0.23	–	7.7	–	–	N
123	344.951	1.096	0.37	0.2	12	3.7×10^4	1.7×10^{22}	N
124	344.906	1.196	0.38	0.2	13	4.5×10^4	2.0×10^{22}	N
125	345.092	1.733	0.36	–	12	–	–	N
126	345.261	1.108	0.42	0.3	14	2.1×10^4	1.2×10^{22}	N
127	345.467	0.419	0.45	0.2	15	4.8×10^4	2.2×10^{22}	N
128	344.801	1.082	0.27	–	8.9	–	–	N
129	345.482	1.233	0.23	–	7.5	–	–	N
130	345.464	1.443	0.21	–	7.0	–	–	Y
131	344.849	1.312	0.24	–	7.9	–	–	N
132	345.484	0.856	0.17	–	5.5	–	–	N
133	345.304	0.435	0.12	–	3.9	–	–	N
134	344.945	1.600	0.64	0.3	21	2.1×10^4	1.4×10^{22}	N
135	344.950	1.587	0.22	–	7.3	–	–	N
136	345.272	1.051	0.36	0.3	12	1.7×10^4	9.8×10^{21}	N
137	345.060	1.727	0.37	–	12	–	–	N
138	345.479	0.400	0.26	–	8.7	–	–	N
139	344.846	1.293	0.21	–	7.1	–	–	N
140	345.909	0.514	0.36	0.2	12	3.4×10^4	1.6×10^{22}	N
141	345.812	1.756	0.26	–	8.5	–	–	N
142	344.957	1.188	0.24	–	7.9	–	–	N
143	345.320	1.417	0.29	0.4	9.6	7.6×10^3	5.5×10^{21}	Y
144	345.869	1.820	0.21	–	6.8	–	–	N
145	345.278	1.112	0.35	0.2	12	2.7×10^4	1.4×10^{22}	N
146	345.634	0.770	0.33	0.2	11	3.5×10^4	1.6×10^{22}	N
147	345.044	1.618	0.32	0.3	11	2.4×10^4	1.2×10^{22}	N
148	344.809	1.075	0.12	–	3.8	–	–	N
149	345.683	1.459	0.30	0.3	9.9	2.2×10^4	1.1×10^{22}	N
150	345.566	0.267	0.17	–	5.7	–	–	N
151	344.925	1.316	0.33	–	11	–	–	N
152	345.699	1.508	0.18	–	5.9	–	–	N
153	345.286	0.412	0.14	–	4.6	–	–	N
154	345.611	0.365	0.27	–	8.8	–	–	N
155	344.916	1.826	0.17	–	5.5	–	–	N

Continued on next page

Table 5 – continued from previous page

Name	Galactic coord. long.	lat.	$S_{1.2mm}$ Jy	Diameter pc	Mass M_{\odot}	Density cm^{-3}	Column density cm^{-2}	Infrared counterpart
156	345.472	0.412	0.22	–	7.2	–	–	N
157	345.038	1.848	0.28	0.2	9.2	2.9×10^4	1.3×10^{22}	N
158	345.792	1.757	0.17	–	5.7	–	–	N
159	345.254	1.012	0.089	–	3.0	–	–	N
160	345.708	1.456	0.24	–	8.0	–	–	N
161	345.472	1.231	0.71	0.4	24	1.3×10^4	1.1×10^{22}	N
162	345.497	1.437	0.19	0.3	6.4	8.0×10^3	5.0×10^{21}	N
163	344.783	1.105	0.28	–	9.3	–	–	N
164	345.638	0.330	0.11	–	3.7	–	–	N
165	345.699	1.853	0.21	–	7.1	–	–	N
166	344.986	1.109	0.10	–	3.4	–	–	N
167	345.018	1.762	0.17	–	5.7	–	–	Y
168	344.893	1.335	0.45	0.4	15	1.0×10^4	7.8×10^{21}	N
169	344.956	1.348	0.47	0.4	16	6.2×10^3	5.6×10^{21}	N
170	345.948	0.723	0.14	–	4.5	–	–	N
171	344.891	1.345	0.20	–	6.6	–	–	N
172	344.924	1.824	0.19	–	6.4	–	–	N
173	344.929	1.610	0.15	–	5.0	–	–	N
174	345.247	0.385	0.18	–	5.9	–	–	N
175	345.547	0.960	0.13	–	4.4	–	–	N
176	344.892	1.847	0.25	–	8.3	–	–	N
177	345.888	1.414	0.26	0.2	8.6	2.3×10^4	1.1×10^{22}	N
178	345.510	0.159	0.095	–	3.2	–	–	N
179	345.418	1.469	0.15	0.2	4.8	1.7×10^4	7.5×10^{21}	N
180	344.920	1.419	0.17	–	5.5	–	–	N
181	345.079	1.847	0.12	–	4.1	–	–	N
182	345.236	1.000	0.20	–	6.6	–	–	N
183	345.375	1.571	0.14	–	4.7	–	–	N
184	345.684	1.516	0.14	–	4.7	–	–	N
185	345.532	1.634	0.13	–	4.3	–	–	N
186	345.697	1.459	0.19	–	6.1	–	–	N
187	345.501	1.415	0.23	0.3	7.5	1.6×10^4	8.2×10^{21}	N
188	345.816	1.765	0.23	–	7.5	–	–	N
189	345.086	1.611	0.32	0.4	11	5.2×10^3	4.4×10^{21}	N
190	345.043	1.838	0.21	0.3	7.0	1.4×10^4	7.5×10^{21}	N
191	345.442	1.572	0.11	–	3.8	–	–	N
192	345.468	1.225	0.13	–	4.2	–	–	N
193	344.951	1.082	0.34	0.3	11	9.6×10^3	6.7×10^{21}	N
194	345.482	0.431	0.27	0.3	8.8	1.9×10^4	9.8×10^{21}	N
195	344.913	1.165	0.13	–	4.4	–	–	N
196	344.933	1.820	0.17	–	5.7	–	–	N
197	345.458	1.559	0.13	0.2	4.5	1.1×10^4	5.3×10^{21}	N
198	345.792	1.440	0.096	–	3.2	–	–	N
199	345.098	1.726	0.11	–	3.7	–	–	N
200	345.293	1.093	0.14	–	4.5	–	–	N
201	344.991	1.150	0.11	–	3.8	–	–	N